# Low-Reynolds Number Aerodynamics of an 8.9% Scale Semispan Swept Wing for Assessment of Icing Effects

Andy P. Broeren[1]
*NASA John H. Glenn Research Center, Cleveland, Ohio, 44135 USA*

Brian S. Woodard[2] and Jeffrey M. Diebold[3]
*University of Illinois at Urbana-Champaign, Urbana, Illinois 61801 USA*

*and*

Frédéric Moens[4]
*ONERA—The French Aerospace Lab, 92190 Meudon, FRANCE*

Aerodynamic assessment of icing effects on swept wings is an important component of a larger effort to improve three-dimensional icing simulation capabilities. An understanding of ice-shape geometric fidelity and Reynolds and Mach number effects on the iced-wing aerodynamics is needed to guide the development and validation of ice-accretion simulation tools. To this end, wind-tunnel testing and computational flow simulations were carried out for an 8.9%-scale semispan wing based upon the Common Research Model airplane configuration. The wind-tunnel testing was conducted at the Wichita State University 7 ft x 10 ft Beech wind tunnel from Reynolds numbers of $0.8\times10^6$ to $2.4\times10^6$ and corresponding Mach numbers of 0.09 to 0.27. This paper presents the results of initial studies investigating the model mounting configuration, clean-wing aerodynamics and effects of artificial ice roughness. Four different model mounting configurations were considered and a circular splitter plate combined with a streamlined shroud was selected as the baseline geometry for the remainder of the experiments and computational simulations. A detailed study of the clean-wing aerodynamics and stall characteristics was made. In all cases, the flow over the outboard sections of the wing separated as the wing stalled with the inboard sections near the root maintaining attached flow. Computational flow simulations were carried out with the ONERA elsA software that solves the compressible, three-dimensional RANS equations. The computations were carried out in either fully turbulent mode or with natural transition. Better agreement between the experimental and computational results was obtained when considering computations with free transition compared to turbulent solutions. These results indicate that experimental evolution of the clean wing performance coefficients were due to the effect of three-dimensional transition location and that this must be taken into account for future data analysis. This research also confirmed that artificial ice roughness created with rapid-prototype manufacturing methods can generate aerodynamic performance effects comparable to grit roughness of equivalent size when proper care is exercised in design and installation. The conclusions of this combined experimental and computational study contributed directly to the successful implementation of follow-on test campaigns with numerous artificial ice-shape configurations for this 8.9% scale model.

---

[1] Research Aerospace Engineer, Icing Branch, 21000 Brookpark Rd., MS 11-2, Associate Fellow AIAA.
[2] Research Associate, Dept. of Aerospace Engineering, 306 Talbot Lab, 104 S. Wright St., Member AIAA.
[3] Graduate Research Assistant, Dept. of Aerospace Engineering, 306 Talbot Lab, 104 S. Wright St., Member AIAA.
[4] Research Engineer, Aerodynamics Aeroelasticity Acoustics Department, 8 rue des Vertugadins.

# I. Introduction

Ice accretion and the resulting aerodynamic effect on large-scale swept wings is an extremely complex problem that affects the design, certification and safe operation of transport airplanes. Broeren et al.[1] describe the current situation where there is increasing demand to balance trade-offs in aircraft efficiency, cost and noise that tend to compete directly with allowable performance degradations over a large range of icing conditions. As a result of these trade-offs combined with the ever-present demand to reduce development cost, there is increasing reliance on computational tools for icing simulation. In addition, NASA is conducting research toward future generations of advanced airplane configurations with ambitious goals to improve efficiency while reducing emissions and noise. This research also relies on the development of advanced icing simulation tools in order to realize these design goals. However, sufficient high-quality data to evaluate the performance of these icing simulation tools on iced swept wings are not currently available in the public domain. This problem is being addressed through a large collaborative research effort sponsored by NASA, the Office National d'Etudes et Recherches Aérospatiales (ONERA) and the Federal Aviation Administration (FAA).

A main objective of this collaborative research effort was accomplished in the year 2016 with the publication of an experimental ice-accretion database for large-scale swept wings.[2] A primary purpose of this database is for the evaluation of three-dimensional icing simulation tools such as those being developed within NASA and ONERA.[3,4] There is an inherent difficulty as to how these comparisons should be conducted because of the large-scale, three-dimensionality associated with the experimental ice accretion in some cases (e.g., "scallops" or "lobster tails"). An important question is how much detail of this three-dimensional geometry is critical to the iced-wing aerodynamics and therefore must be accurately simulated. One possible comparison metric is the resulting potential aerodynamic degradation of the swept-wing. Therefore, the remaining objectives of the larger, collaborative research effort are to:

- Develop a systematic understanding of the aerodynamic effect of icing on swept wings including: Reynolds and Mach number effects, important flowfield physics and fundamental differences from 2-D.
- Determine the level of ice-shape geometric fidelity required for accurate aerodynamic simulation of swept-wing icing effects.

The approach used to accomplish these objectives has been successfully carried out in previous icing aerodynamics studies of straight wings and airfoils.

In past work, geometric representations of ice accretion have been attached to wings and models and tested in dry-air wind tunnels or in flight. These geometric representations are known as "artificial ice shapes" or "ice-accretion simulations." The various methods and geometric fidelities associated with developing artificial ice shapes has been investigated in a previous NASA-ONERA collaborative research effort called "SUNSET1."[5] Since that time, a new approach for producing high-fidelity artificial ice shapes has been developed using 3-D scanning and rapid-prototype manufacturing (RPM).[6] In past studies of icing performance effects on airfoils, systematic investigations of Reynolds and Mach number effects were conducted.[7-13] Over the course of many years, it was found that aerodynamic tests conducted in the Reynolds number range of 1.0 to $2.0 \times 10^6$ could yield results applicable to flight Reynolds number (e.g., 10 to $20 \times 10^6$) for leading-edge ice shapes. Therefore, the current research effort will determine if similar trends apply for full-span, leading-edge ice on a swept wing. This effort involves both low- and high-Reynolds number aerodynamic testing. The low-Reynolds number aerodynamic testing is being conducted in the Wichita State University (WSU) 7-ft x10-ft size atmospheric wind tunnel. The high-Reynolds number aerodynamic testing is being conducted in the ONERA F1 11.4-ft x 14.8-ft pressurized wind tunnel using a model 1.5 times larger in geometric scale. The pressurization capability of this facility will allow for independent variations in Reynolds number up to approximately $12 \times 10^6$ and Mach number up to approximately 0.36. The results from the ONERA F1 test campaigns will be analyzed for Reynolds and Mach number effects (among other things) and compared to the results of the WSU test campaigns to determine the extent to which iced, swept-wing aerodynamic testing can be conducted in smaller-scale facilities at lower Reynolds number.

The purpose of this paper is to present the results of the low-Reynolds number swept-wing characterization conducted to date with complementary computational fluid dynamics (CFD) simulations. This work has the following specific objectives:

- Evaluate splitter plate configurations suitable for both the 8.9% scale, low-Reynolds number and the 13.3% scale high-Reynolds number aerodynamic wind-tunnel models.
- Generate a preliminary experimental and computational assessment of low-Reynolds number, swept-wing performance in the clean configuration for baseline data and with artificial ice roughness to determine expected aerodynamic sensitivity prior to the first F1 campaign.

- Evaluate the ability of RPM methods to fabricate small-size roughness features with sufficient accuracy such that they can be instrumented and attached accurately and precisely to the leading edge of the 8.9% scale wing.

In order to carry out these objectives, aerodynamic testing was conducted at the WSU 7x10 wind tunnel using the 8.9% scale semispan wing model of the CRM65. The CRM65 geometry is based upon the Common Research Model (CRM) described in previous papers[1,14-17] and in Section II.B. Different wing mounting configurations were tested with and without various splitter plate combinations. The aerodynamic results were analyzed and a final mounting configuration was selected for the remainder of the test campaign. CFD simulations were performed for this final configuration with a free-transition model and fixed transition. Artificial ice roughness was designed using regular patterns of hemispherical geometry. This was incorporated into the removable portion of the wing leading-edge geometry and fabricated using stereo-lithography. The resulting artificial ice shapes were instrumented to measure surface static pressure. Silicon-carbide grains were also used to simulate small ice roughness. Grit sizes equivalent to the hemispherical roughness sizes were applied to the wing leading edge. Aerodynamic performance testing was conducted in angle of attack sweeps over a Reynolds number range of $0.8\times10^6$ to $2.4\times10^6$ and a corresponding Mach number range of 0.09 to 0.27. Force-balance and surface-pressure data were acquired. Surface-oil and mini-tuft flow visualization techniques were employed for a subset of the configurations. This paper documents the important aerodynamic characteristics of this wing and test-section installation. The companion papers by Camello et al.[18] and Lum et al.[19] provide more results regarding the effect of artificial ice shapes on the wing aerodynamic performance and flowfield.

## II. Wind-Tunnel Facility, Model and Experimental Methods

### A. Wind-Tunnel Facility

All experiments were carried out in the Walter H. Beech Wind Tunnel at Wichita State University. The tunnel is an atmospheric, closed-return type, subsonic wind tunnel with a 7 ft x 10 ft test section. The maximum speed of the tunnel is approximately 350 ft/s which corresponds to a Reynolds number per foot of approximately $1.8\times10^6$ and a maximum dynamic pressure of 125 psf. The dynamic pressure was controlled to within ±0.1 psf over the entire operating range. The freestream turbulence intensity in the central region of the test section is approximately 0.07% of the freestream velocity. Force balance and surface pressure measurements were acquired at Reynolds numbers of $0.8\times10^6$, $1.6\times10^6$ and $2.4\times10^6$ which corresponded to freestream Mach numbers of 0.09, 0.18 and 0.27. The speed control was based upon Reynolds number, therefore small differences in Mach number were observed. For example, the Mach number corresponding to $Re = 1.6\times10^6$ varied between 0.17 and 0.18. The model angle of attack was varied from -6 deg to 16 deg. The specific angle of attack schedule was adjusted depending upon the model configuration. In some cases, a fine angle of attack resolution of 0.2 deg was required to capture certain aerodynamic features.

Load measurements were performed using a 6-component pyramidal style force balance located beneath the test section floor. This study utilized a reflection plane model and the force balance was used to measure the lift, drag and pitching moment. The force balance does not directly measure the lift and drag but rather it measures the normal force and the axial force which are relative to a coordinate system fixed to the force balance. A coordinate rotation is required to determine the lift and drag in the wind axes.[20] The force balance measures the moment about a reference point fixed to the force balance and it is necessary to transfer the moment to the reference point on the model. For the model used in this study there was an offset along the x-axis of the force balance between the balance reference point and the model reference point. The model center of rotation and moment center are defined in Section II.B, below. The accuracy of the balance was 0.02% of full-scale. The uncertainty in the measured dynamic pressure was approximately ±0.1 psf.

Surface pressure measurements were acquired using miniature electronic pressure scanning (ESP) modules developed by Esterline (model ESP-32HD). An ESP module with a range of ±10.0 psi was used for pressure taps located near the leading edge of the model. For the remaining pressure taps a module with a range of ±2.0 psi was used. The accuracy, in percent of full-scale, was ±0.03% and ±0.06% for the 10 psi and the 2 psi module, respectively. This corresponds to an uncertainty of ±0.003 psi and ±0.0012 psi for the two modules.

The uncertainties in the experimental data were determined using the standard "root-sum-square" (RSS) method outlined by Coleman and Steele[21] and developed by Kline and McClintock.[22] These uncertainties were estimated for 20:1 odds and use the numerical values for the instrumentation described in the preceding paragraphs. More details of this analysis are reported in Ref. 23. Table 1 provides a summary of the absolute and relative uncertainties in the wing angle of attack and performance coefficients calculated for an example point at α = 4 deg with $Re = 2.4\times10^6$ and $M = 0.27$ All of these values were considered acceptable for this work.

**Table 1. Absolute and Relative Uncertainties for Example Data Point Acquired at $Re = 2.4 \times 10^6$ and $M = 0.27$.**

| Variable | Reference Value | Absolute Uncertainty | Relative Uncertainty |
|---|---|---|---|
| $\alpha$ | 4.00 deg | ±0.05 deg | ±1.25% |
| $C_L$ | 0.5029 | ±0.00137 | ±0.27% |
| $C_D$ | 0.0215 | ±0.00068 | ±3.15% |
| $C_M$ | -0.0067 | ±0.0006 | ±9.01% |

All aerodynamic data ($\alpha$, $C_L$, $C_M$, $C_D$ and $C_p$) presented in this paper were corrected for wind-tunnel-wall effects using the standard procedure for 3D models outlined in Barlow et al.[24] as implemented by Wichita State University.[25] It should be noted that these corrected results are considered preliminary. The standard wind tunnel-wall corrections for swept-wing, reflection-plane models involve numerous assumptions that require further evaluation as to their suitability for the performance data to be acquired in the planned test campaigns, particularly with respect to the wing with leading-edge ice shapes.

As described in Section I, aerodynamic data acquired at the WSU wind tunnel will be compared with data acquired at the ONERA F1 facility. Therefore, it is important that the effect of the wind-tunnel walls on the aerodynamic data from both facilities be accounted for properly. In addition, CFD simulations will also be performed and compared to the experimental results. Wall corrections on the experimental data will also be important for comparison to CFD simulation results that do not model the presence of the wind-tunnel walls. References 23 and 24 provide a description of the primary wind tunnel-wall effects and the potential limitations of the correction procedure used for the data in this paper.

**B. Wind-Tunnel Model Description**

The semispan model fabricated for these wind-tunnel tests was based on an 8.9% scale version of the CRM65 wing. The full-scale CRM65 geometry has a realistic cruise configuration loading applied to the wing resulting in a wing shear similar to dihedral.[14] In order to simplify the design of the removable leading edge segments (described below), this shearing or "bending" of the wing was removed from the model geometry resulting in an unsheared wing with a straight leading edge across the span of the model. The wing retains the twist and taper of the CRM65. Table 2 summarizes the geometric parameters of the wing, and a diagram of the CRM planform is shown in Fig. 1 with key dimensions. The model was machined from aluminum and contained 219 pressure taps in its clean configuration. Figure 2 shows a computer-aided design (CAD) model of the wing and all of its components along with a photograph of the wing installed in the wind tunnel with the circular splitter plate.

This model was designed and built with a removable leading edge that allows artificial ice-shapes to be added to the wing. This approach has been used in previous icing aerodynamic studies[5,10,12,13] and allows for very efficient and repeatable changes in the artificial ice-shape configurations. This is important for this research effort, since many different ice-shape configurations are being investigated. The machined, aluminum portions of the model consist of the main element (including a spar that attaches to the force balance), a full-span clean leading edge, and a partial-span leading edge used for mounting ice shapes. An open channel exists between the main element and any of the leading-edge components for routing pressure tubing out the base of the model to the data acquisition system. The seam between the clean leading edge and the main element is a straight line on both the upper and lower surfaces, but the seam is not at the same location on both surfaces. Typically, ice accretes farther back on the wing of an aircraft on the lower surface than the upper surface, so the lower surface artificial ice shapes cover a greater portion of the local chord. At the root of the wing, the seam is at 9.3% and 22.8% of the local streamwise chord on the upper and lower surfaces, respectively. At the tip of the wing, the seam is at 14.8% and 40.6% of the local streamwise chord on the upper and lower surfaces, respectively. The seam between components along the upper surface of the model can be seen in Figs. 2 and 3.

When artificial ice shapes including ice roughness were mounted on the wing for testing, the partial-span removable leading edge was used to attach some of those pieces. The partial-span removable leading edge extends from the root to just beyond half the span of the model, and it contains a portion of the airfoil contour on the lower surface. Artificial ice shapes were attached to this removable leading edge and covered the entire upper surface of this removable leading edge. No pressure taps were added to this leading edge. Outboard of this partial-span leading edge, the artificial ice shapes were attached directly to the main element. The reason for this is that the model thickness decreases significantly on the outboard portion of the wing. There is not enough material to extend the removable leading edge. This design does not adversely affect the efficiency or repeatability of the artificial ice-shape configuration changes. The artificial ice shapes and roughness were created using an RPM technique called stereo-lithography. For these tests, the artificial ice roughness configurations on the removable leading edge were

divided into six, approximately equal length segments. Each of the segments consisted of approximately 12.5 in of the swept leading edge of the wing. Pressure taps were installed in each of these segments at the same locations as on the clean aluminum leading edge. The pressure tap holes were included in the RPM design, and then steel tubes were glued in to each hole and plumbed to the quick disconnect. Each of the separate RPM components is shown in a different color on the full model in Fig. 3.

**Table 2. Summary of 8.9% Scale CRM65 Semispan Wing Geometric Parameters**

| Wing Parameter | Value |
|---|---|
| Span | 5.00 ft (60.00 in) |
| MAC | 1.39 ft (16.67 in) |
| Area (Geometric) | 6.01 ft$^2$ (865.3 in$^2$) |
| Volume | 0.617 ft$^3$ (1069 in$^3$) |
| Aspect ratio* | 8.3 |
| Taper ratio | 0.23 |
| Root chord | 2.25 ft (27.00 in) |
| Tip chord | 0.52 ft (6.19 in) |
| Root $\alpha$ | 4.4 deg. |
| Tip $\alpha$ | -3.8 deg. |
| 1/4-chord sweep angle | 35 deg. |
| Leading edge sweep angle | 37.2 deg. |
| Location of rotation center[†] | $x = 19.368$ in., $z = 0$ |
| Location of moment center[†] | $x = 23.868$ in., $z = 0$ |

*--While the other parameters in this table are defined specifically for this model, the aspect ratio is defined for a complete airplane configuration using the formula, $\frac{(2 \, x \, semispan)^2}{2 \, x \, area \, of \, one \, wing}$.

[†]--(0, 0, 0) is the wing root-section leading edge at zero angle of attack.
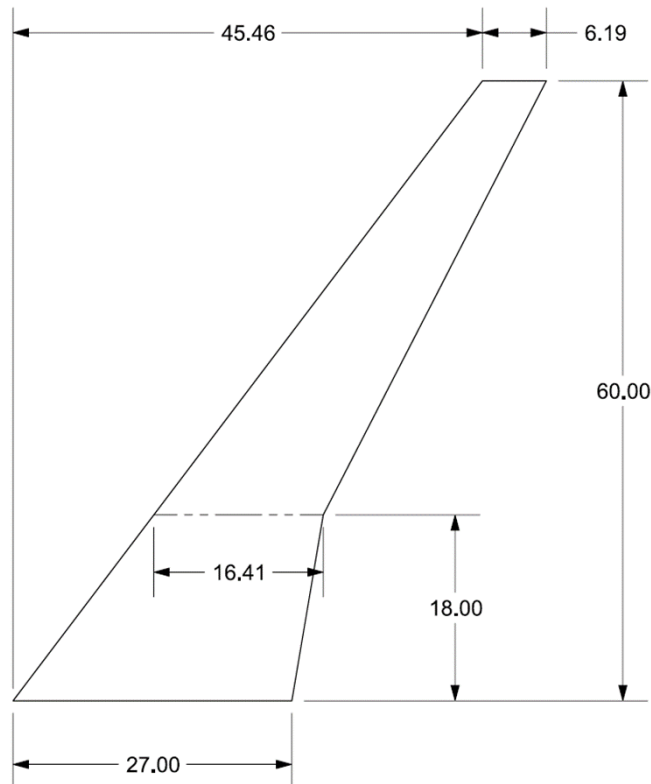


**Figure 1. 8.9% scale CRM65 semispan wing planform with key dimensions labeled in inches.**
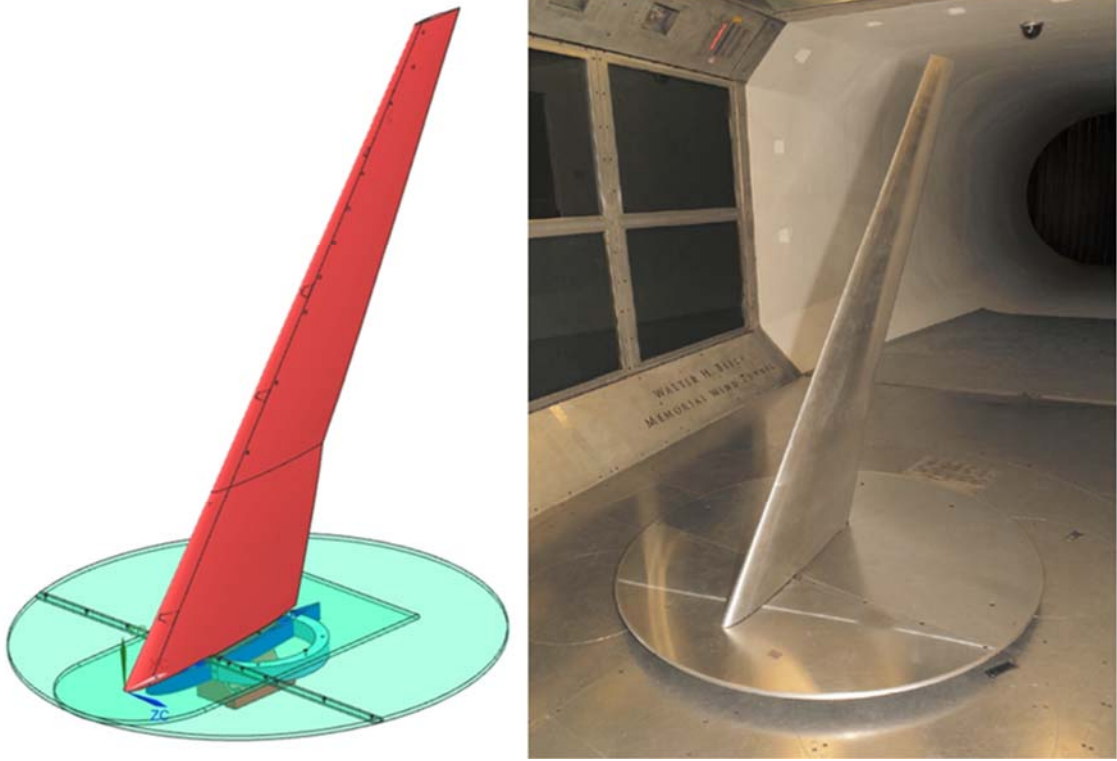
**Figure 2. CAD model of wing (left); wing installed in WSU wind-tunnel test section (right).**
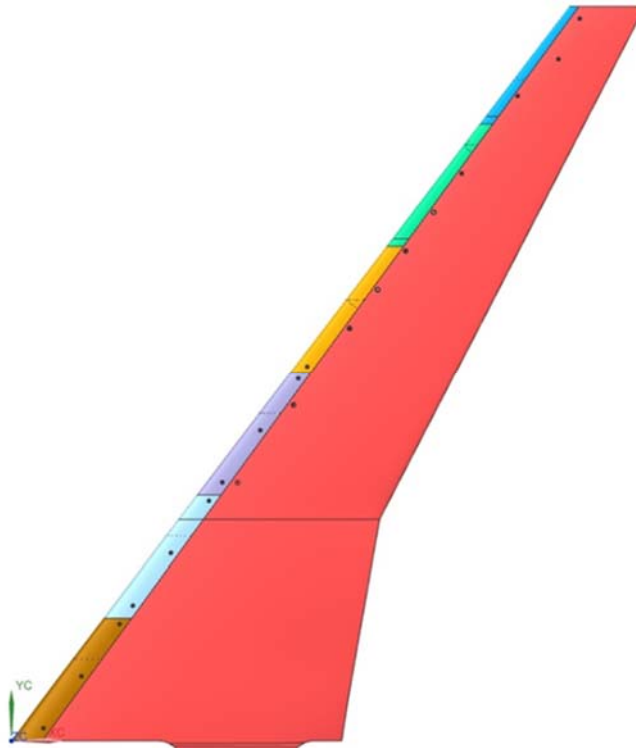


**Figure 3. CAD model of wing with each removable ice-shape leading edge segment highlighted.**

American Institute of Aeronautics and Astronautics

The 219 pressure taps in the model were distributed in 10 different rows.  Some rows were oriented normal-to-the-leading edge, and others were in the streamwise direction.  The tap rows were identified by the spanwise location of the tap located at the leading-edge hilite.  The spanwise position of subsequent taps changes in the normal-to-the-leading-edge rows.  Further information regarding each of the tap rows can be found in Table 3 and the tap row locations are shown graphically in Fig. 4.  The streamwise tap rows each contained upper- and lower-surface taps as well as a tap located at the leading edge of that row.  The normal-to-the-leading-edge taps only contained pressure taps on the upper surface, and they did not extend all the way to the leading edge.  The taps closest to the leading edge from the streamwise row were used to complete the normal row when plotting the data.  The taps in the main element of the model were plumbed with stainless steel tubing from their location on the surface out the root of the model.  The taps in the leading edge required a more complicated route.  The stainless steel tubing in both the clean leading edge and in the RPM ice leading edges transitioned to plastic tubing and then connected to a Scanivalve quick disconnect fitting.  The use of these fittings allowed relatively quick model reconfigurations between clean and RPM leading edges.

**Table 3.  Details of the Pressure Tap Instrumentation**

| Row Identifier | Orientation | Spanwise Location* $y/b$ | in | Taps in RLE | Upper Surface | Lower Surface | Total Taps |
|---|---|---|---|---|---|---|---|
| 1 | Normal | 0.11 | 6.6 | 3 | 12 | 0 | 12 |
| 2 | Streamwise | 0.11 | 6.6 | 13 | 19 | 11 | 31 |
| 3 | Streamwise | 0.28 | 16.8 | 13 | 18 | 11 | 30 |
| 4 | Normal | 0.44 | 26.4 | 4 | 16 | 0 | 16 |
| 5 | Streamwise | 0.44 | 26.4 | 12 | 18 | 10 | 29 |
| 6 | Normal | 0.60 | 36.0 | 4 | 16 | 0 | 16 |
| 7 | Streamwise | 0.60 | 36.0 | 13 | 18 | 10 | 29 |
| 8 | Normal | 0.81 | 48.6 | 4 | 16 | 0 | 16 |
| 9 | Streamwise | 0.81 | 48.6 | 13 | 18 | 10 | 29 |
| 10 | Streamwise | 0.90 | 54.0 | 3 | 11 | 0 | 11 |

*--Spanwise location is provided for the leading edge taps for Rows 1, 3, 6, and 8 that were oriented normal to the leading edge.
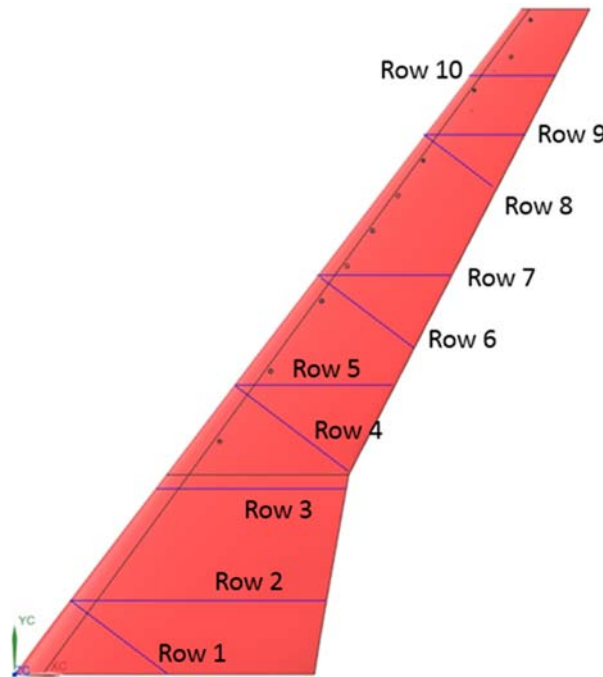


**Figure 4.  Pressure tap row locations on wing upper surface.**

## C. Splitter Plate and Shroud Configurations

In addition to the actual wing model, several auxiliary pieces were designed for testing during this test campaign. A system of splitter plates was developed to evaluate the effect of model-installation configuration on the wing aerodynamic performance. Mounting with a splitter plate was selected over a half-fuselage configuration for several reasons including cost, complexity and concerns about increased blockage. The splitter plates were designed based upon earlier work with a similar model, but at smaller scale.[26] When testing with a splitter plate, the model is raised out of the wind-tunnel floor boundary layer. A new boundary layer forms on the splitter plate, but the splitter plate geometry is well established and can be repeated in different wind-tunnel facilities. The differing floor boundary layers between various wind tunnels becomes a reduced concern when comparing data if a consistent splitter plate is utilized. The splitter-plate system consisted of the splitter plate itself and a shroud that held the splitter plate above the test-section floor and shielded the model spar from aerodynamic loads. Neither the splitter plate nor the shroud were connected to the model or the force balance. They were mounted to the turntable, so both pieces moved with the model. Two configurations of each of the two components were designed for this test. Each piece had a circular cross-section version that presented a constant geometry even as the angle of attack of the model changed, and each piece also had a smaller, lower blockage version. The smaller splitter plate was generally rectangular and the smaller shroud was streamlined in shape as a NACA 0018 airfoil. A model of the splitter plates and the wing is shown in Fig. 5 with each of the components labeled. Both of the splitter plates were designed such that they extended 25% of the root chordlength upstream of the leading edge of the model. The distance from the center of rotation of the model to the root leading edge set the diameter of the circular splitter plate. The rectangular plate also extended 25% of the root chord downstream of the root of the model and was five times the width of the maximum root-section thickness. For structural reasons, the plates were 0.5 in thick, and the edges of the plates were rounded. The edge radius design was shown in previous work[26] to reduce boundary-layer separation on the surface of the splitter plate. The gap between the bottom of the splitter plates and the wind-tunnel floor was 2.0 in based on floor boundary-layer data provided by the WSU wind-tunnel facility. Due to the location of the wing spar relative to the center of rotation of the model, the circular shroud had to be relatively large with a diameter of 14.75 inches. The blockage from the circular shroud did not change with angle of attack, but the blockage under the splitter plate did change with angle of attack in the streamlined-shroud configuration. All of the components of the splitter-plate system were designed to be removed without affecting the model mounting, so that the configurations could easily be tested. Figure 6 shows the splitter-plate system with the key dimensions illustrated. The wing is not shown in Fig. 6, but the coordinate system indicates the location of the root leading edge. In the case without a splitter plate, the model had to be lowered by 2.5 inches. These changes were accomplished using a spacer block between the model spar and the force balance.
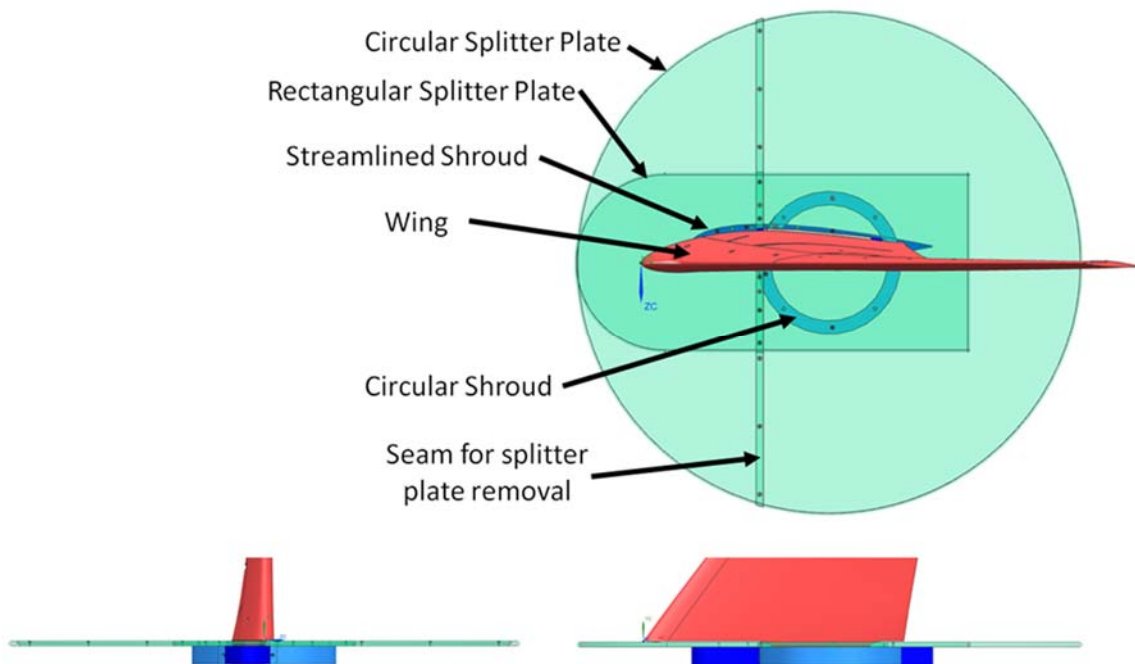


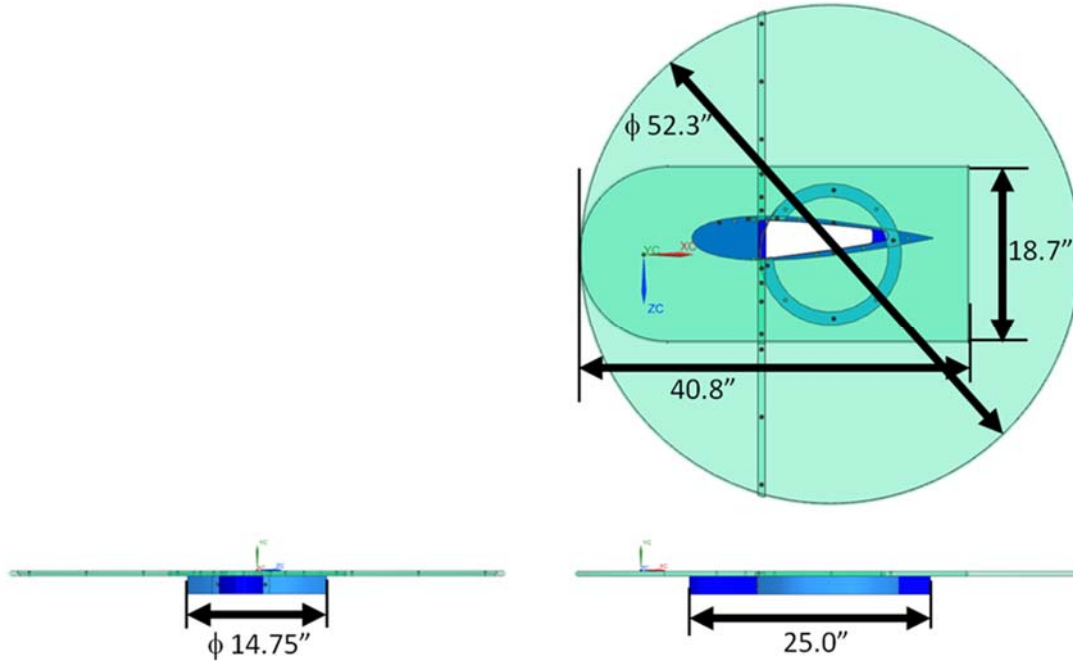**Figure 5. Multiple model views of the splitter plate system and wing with each component labeled.**

American Institute of Aeronautics and Astronautics

**Figure 6. Multiple model views of the splitter plate system without the wing showing key dimensions in inches.**

## D. Boundary-Layer Trip Configurations

The model was tested with boundary-layer trips applied near the leading edge on both upper and lower surfaces of the wing. These tests were conducted to facilitate comparison with data from future test campaigns at the ONERA F1 wind tunnel and with CFD simulations. The lower-surface trip was comprised of 0.0114 in thick CADCUT "dots". The CADCUT trip dots were 0.050 in diameter circles spaced 0.10 in between centers. The lower-surface trip location was determined by measuring the surface length from the leading-edge hilite perpendicular to the leading edge. At tap Rows 1, 6 and 8 these distances were 2.0, 1.37 and 1.21 in, respectively. The upper-surface trips were located very close to the hilite along the span of the leading edge. For the $Re = 0.8 \times 10^6$, $M = 0.09$ condition, the upper-surface trip was comprised of 0.004 in thick CADCUT trip dots with the same diameter and spacing as on the lower surface. For other two Reynolds and Mach number conditions, the upper-surface trip was comprised of a 0.0025 in thick by 0.25 in wide continuous strip of flash tape. The the leading-edge hilite was located by the forward-most pressure tap installed in each row.

## E. Artificial Ice Roughness Representations

In addition to the clean aluminum machined leading edge, several other leading-edge configurations were tested. As described in Section II.B, six segments along the leading edge could be produced using RPM techniques to represent various potential ice shapes. All of the RPM leading edges were created using stereolithography and were produced by the company Realize, Inc. The stereolithography process utilizes an ultraviolet laser to solidify liquid polymer resins, and the specific polymer chosen for these components was Accura 60. Tolerances are advertised to be ±0.005 in for this process. The tolerances associated with machined aluminum are smaller than the RPM processes, and the RPM leading edges have five seams across the span of the model that were not present in the aluminum leading edge. It should be noted that as an outcome of this work, later test campaigns used a design that reduced the number of spanwise segments from 6 to 2, thus resulting in only one seam near the model midspan. This is described in the companion paper by Camello et al.[18]

An objective of this investigation was to determine the ability of the RPM approach to capture small ice roughness features. Two aspects were involved in this portion of the test. First, the size of the roughness that can accurately be produced using RPM techniques had to be explored, and then the roughness had to be applied to the model to investigate the aerodynamic effects. To simulate ice roughness in the RPM ice shapes, hemispheres were added to the clean-wing leading-edge geometry. The roughness size, $k$, corresponds to the radius of the hemisphere, and a pattern of hemispheres was applied to the leading edge such that the spacing between the center of any two hemispheres was 1.3 times the diameter of the hemispheres. Figure 7 provides a two-dimensional cartoon of this

American Institute of Aeronautics and Astronautics

configuration.  The coverage on the upper and lower surfaces was determined using the impingement limits from the previous LEWICE3D simulations.[1]  As the figure illustrates, the roughness covered a greater portion of the lower surface than the upper surface.

The CAD model pattern of hemispheres on one leading-edge segment is shown in Fig. 8 along with a close-up view of the roughness pattern.  The image on the left shows approximately 7.5 in of the span, and $k = 0.020$ in in this case.  For reference, the pressure tap holes that are shown have a diameter of 0.050 in.  After consultation with Realize, Inc. and the production of several test specimen, the smallest hemispheres that were applied to the entire leading edge had $k = 0.010$ in.  A photograph of a completed RPM-section is shown in Fig. 9.
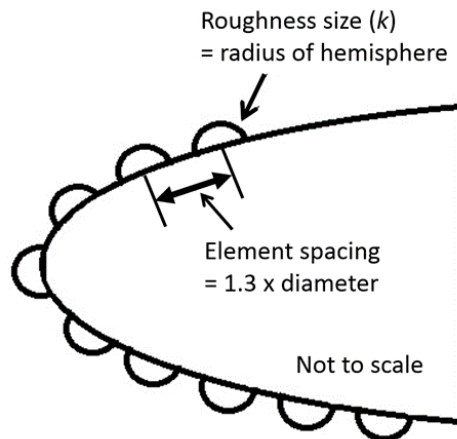


**Figure 7.  Diagram of hemisphere roughness pattern on wing leading edge.**
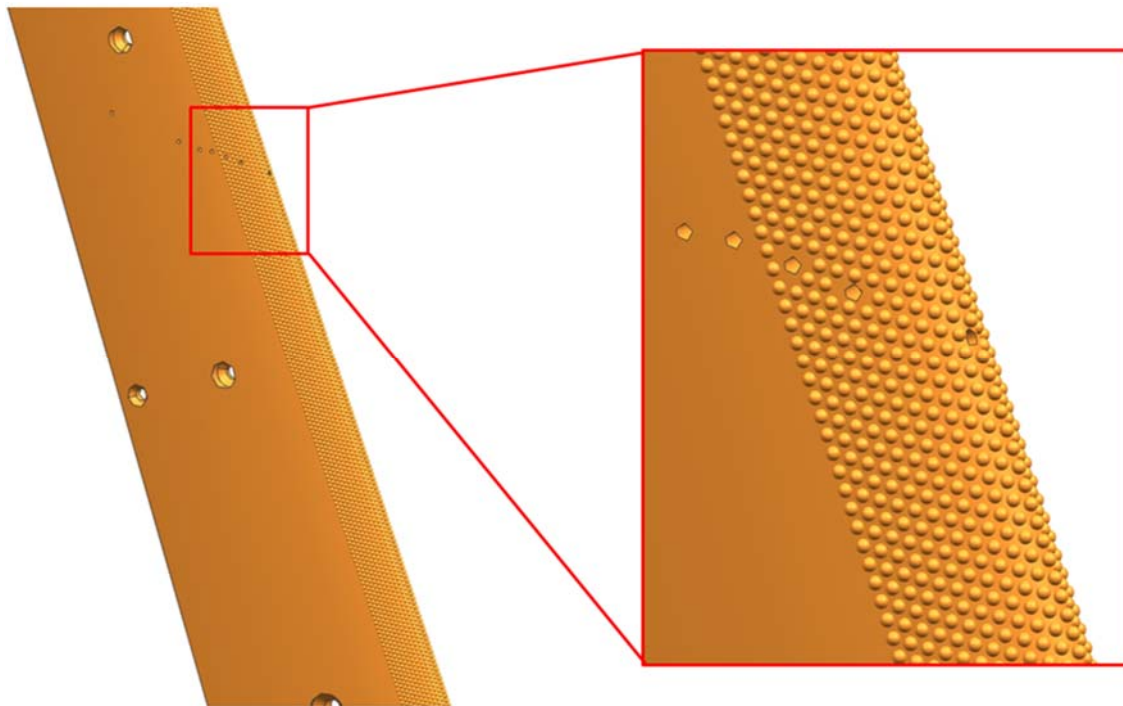


**Figure 8.  CAD model pattern of hemispheres on wing leading edge.**
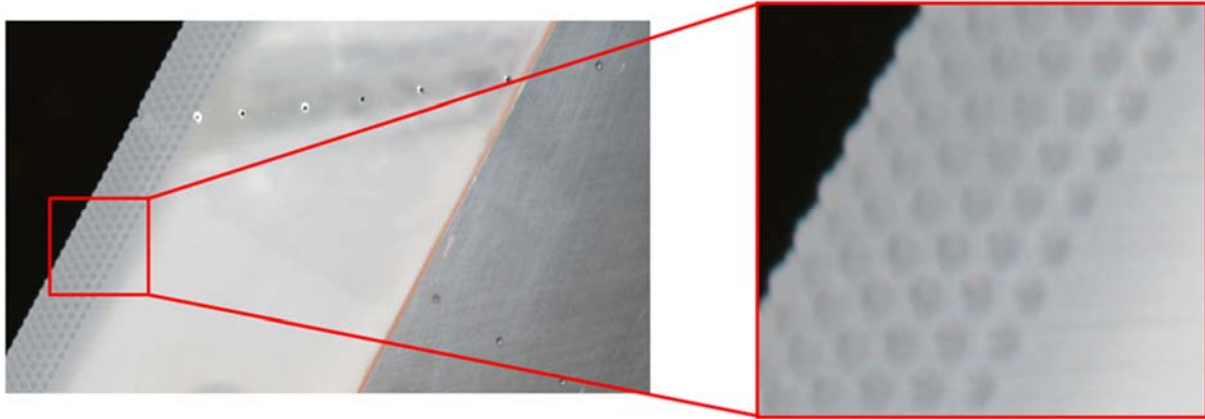
**Figure 9. Photograph of roughness on RPM section of wing leading edge.**

Silicon-carbide grit was also applied to the clean, aluminum leading edge of the model for comparison to the results from the RPM roughness simulations. The grit was applied to the model using double-sided tape, and the extent coverage on the upper and lower surfaces was the same as for the RPM roughness. Two different configurations were used with the grit. In one, the entire span was covered with the grit and tape, and in the other, gaps were left at the pressure tap rows in order to acquire that data. Figure 10 contains photographs of the grit on the double-sided tape before and after it was applied to the model.

The three roughness sizes that were applied to the model during these tests are summarized in Table 4. The CRM65 roughness size represents the equivalent full-scale size of the roughness features. This means that any full-scale roughness elements smaller than 0.056 in could not be captured on the 8.9% scale model used in this work. The table also indicates the type of roughness applied to the model during these tests.
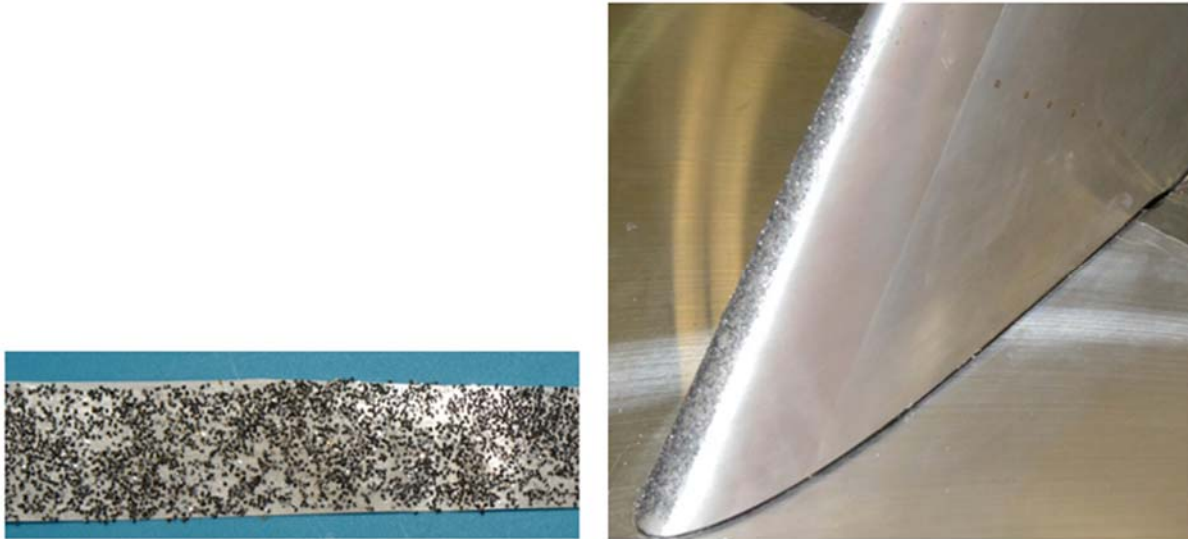


**Figure 10. Grit on tape before (left) and after (right) being applied to wing leading edge.**

**Table 4. Roughness Sizes Applied to Wing Leading Edge**

| CRM65 Roughness Size (in) | Low-Re Roughness Size (in) | $k/c_{mac}$ | Application Configuration |
|---|---|---|---|
| 0.056 | 0.005 | $3.1 \times 10^{-4}$ | Grit |
| 0.112 | 0.010 | $6.3 \times 10^{-4}$ | RPM / Grit |
| 0.225 | 0.020 | $12.5 \times 10^{-4}$ | RPM / Grit |

American Institute of Aeronautics and Astronautics

### F. Flow Visualization

Two flow visualization methods were employed in this work. Fluorescent mini-tufts were applied to the model upper surface for many of the test configurations. The mini-tuft images were acquired during the aerodynamic performance sweeps of the various model configurations. Surface-oil flow visualization was also performed. This flow-visualization method was performed separately from the performance sweeps and only for a limited number of model configurations and angles of attack.

The mini-tufts were made from 0.0019-inch diameter monofilament material dyed with a bright yellow fluorescent pigment. They were applied in streamwise rows and were approximately one inch long. There were held to the surface with cyanoacrylate adhesive. The size of the mini-tuft and adhesive were small and considered to be non-intrusive. Aerodynamic data with and without mini-tufts were compared to ensure that the tufts did not influence the wing performance. The tufts were photographed at selected angles of attack with illumination via a remote flash with UV black light filter. The mini-tuft images provide some insights as to the three-dimensional flow characteristics over the wing upper surface.

Surface-oil flow visualization was performed by applying a mixture of mineral oil and fluorescent dye to the surface of the wing. Prior to applying the oil to the model, the surface was covered with black contact paper. The black surface of the contact paper provided high contrast between the model surface and the fluorescent oil. The fluorescent oil was applied using sponge paint rollers. After the application the test section was closed and the desired wing angle of attack was set. The wind tunnel was set to ramp up to the desired speed. The total time required from fan on to fan off was two minutes. The test section was then accessed for still images acquired with UV-blacklight illumination. The surface oil was then re-distributed into a uniform pattern using the same paint-roller method. This technique can be used to detect features such as separated flow, vortices and laminar-to-turbulent transition that affect the shear forces on the wing surface.

## III. Computational Fluid Dynamics Simulations

### A. Wing Configuration and Grid Generation

The configuration considered for the CFD simulations presented here was based on the WSU wind-tunnel setup. It includes the wing model, the circular splitter plate and the tunnel floor, represented computationally as a symmetry plane (cf. Fig. 2). The other tunnel walls and the shroud element were not considered here. The chimera overset grid technique has been used according to an ONERA methodology for complex configurations.[27] Three individual structured multiblock grids were generated using Pointwise V17 software as depicted in Fig. 11: for the clean wing (~$9.4\times10^6$ cells), for the circular splitter plate (~$6.5\times10^6$ cells) and for the collar grid making the junction between the wing and the plate (~$0.65\times10^6$ cells).
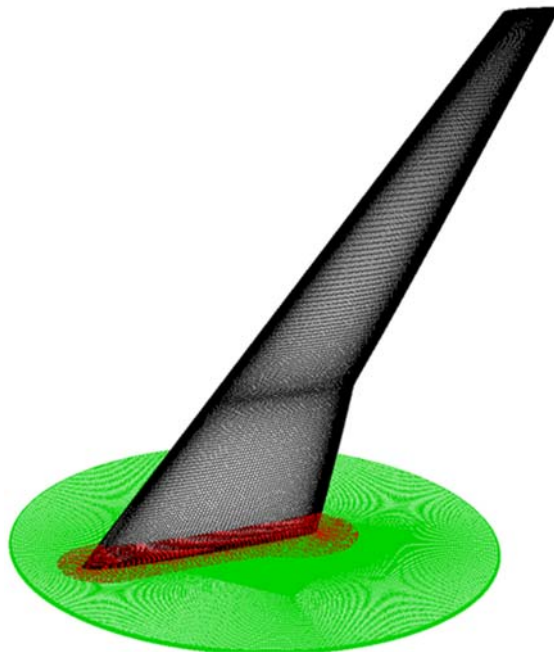


**Figure 11. Surface grids generated for the wing (black), the plate (green) and the collar junction (red).**

The three grids were embedded into a Cartesian background grid, generated using the octree technique. The resulting total number of points was about $44.9 \times 10^6$ before applying the chimera masking process. This post-processing has been carried out using the ONERA Cassiopée[28] suite. Figure 12 gives an example of the resulting grid assembly from this post-processing, with a cut at a constant streamwise ($x$) location.

As the same grid has been used for computations for the different Reynolds and Mach number flow conditions, the y+ values obtained at the walls have been verified for the different Reynolds numbers. As shown in Fig. 13, the values were slightly higher than 1.3 at the wing leading-edge for the highest Reynolds number considered. For the other flow conditions, y+ was around 1 for $Re = 1.6 \times 10^6$ and 0.5 for $Re = 0.8 \times 10^6$, which was quite satisfactory for the Spalart-Allmaras turbulence model described in Section III.B below.
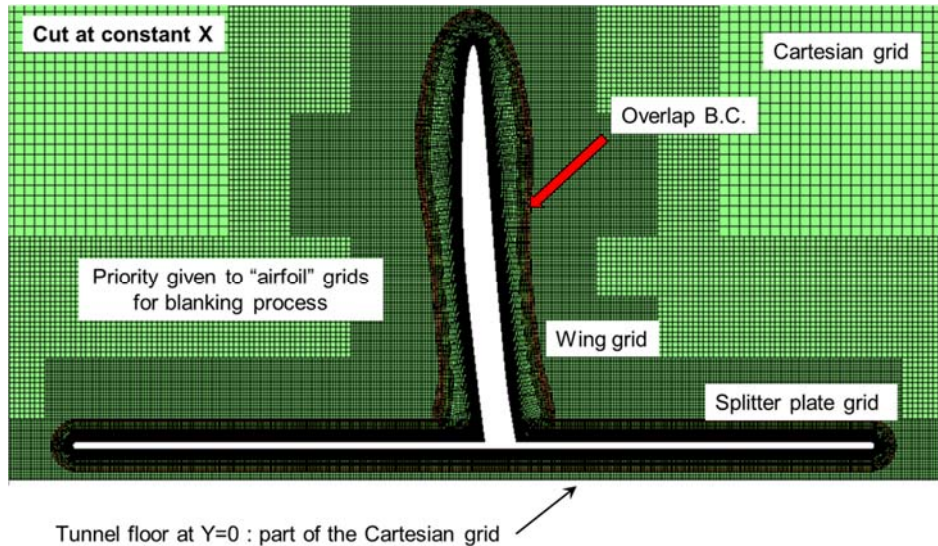


**Figure 12. Cut of the resulting chimera grid used for the CFD computations.**



| $Re = 0.8 \times 10^6, M = 0.09$ | $Re = 1.6 \times 10^6, M = 0.18$ | $Re = 2.4 \times 10^6, M = 0.27$ |
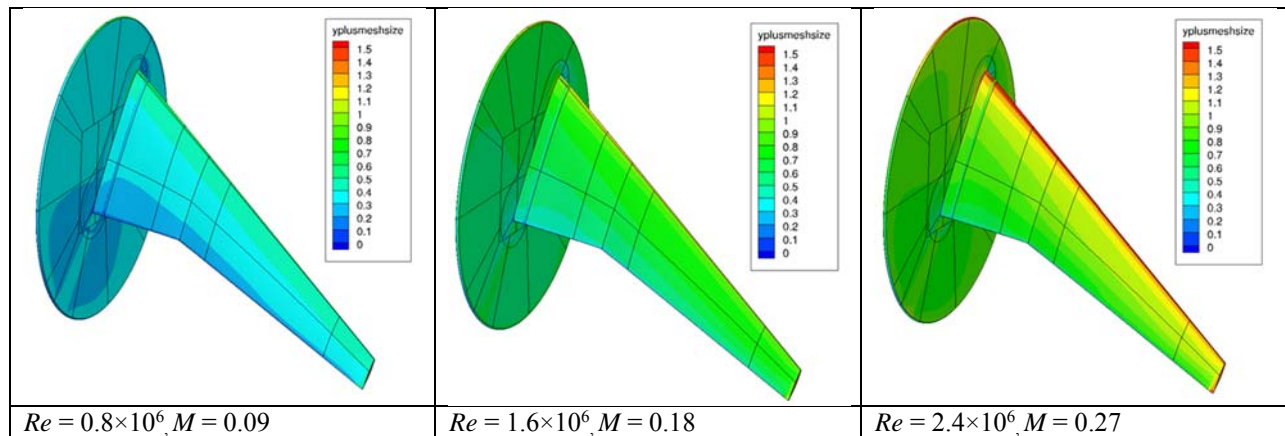
**Figure 13. Reduced height at wall (y+) for the three flow conditions considered ($\alpha_{geo}$ = 5 deg).**

## B. CFD Solver

The CFD solver used in this study is the ONERA elsA solver.[29] The elsA software solves the compressible three-dimensional Reynolds-Averaged, Navier-Stokes (RANS) equations by using a cell-centered finite volume spatial discretization on structured multi-block meshes. For the spatial scheme, the one proposed by Jameson,[30] was used for the conservative variables. A fourth order linear dissipation k4 is generally used, with added second order dissipation terms k2 for treatment of flow discontinuities. In the present study, k2 was set to zero due to the low free-stream Mach number and a low value of k4 coefficient (k4=1/64) has been used for accurate solutions. For the implicit stage, a LUssor scheme is associated with an Euler backward time integration scheme, which allows fast convergence rates. For the turbulent variables, an extension to the second order of the Roe numerical scheme was

used with a Harten entropic correction coefficient set to 0.01 and the "minmod" limiter. Multi-grid computations and low-speed preconditioning have been used for convergence acceleration.

The turbulence model used is the one-equation Spalart-Allmaras[31] one with the Quadratic Constitutive Relation (QCR) correction. Computations were carried out either in fully turbulent mode or with natural transition taken into account.[32] For longitudinal instabilities, a combination of the Arnal-Habiballah-Delcourt[33] and Gleyzes[34] criteria was used, which is applicable to a large flow range from accelerated flows to laminar separation bubbles. For crossflow, the C1 criterion[35] was used. The flow was considered turbulent when any of the two criteria was satisfied. The upstream turbulence rate and the turbulence rate outside the boundary layer were set to 0.11% corresponding to $N_T = 8$ for transition onset. This value corresponds to the measured turbulence level of the WSU wind tunnel. These criteria are functions of the incompressible shape factor $H_i$, of an averaged Pohlhausen parameter $\Lambda_2$, of the cross-flow displacement integral length $\delta_2$, and of the external turbulence level $T_u$. Integral lengths were directly computed from the velocity field, but the shape factor was obtained indirectly as a function of the Pohlhausen parameter. Therefore, standard grid resolutions can be used. In the laminar part of the flow, the intermittency function was set to zero, then turbulence starts, usually some distance downstream of the detected transition location. During the general iterative convergence process, the transition locations were computed and updated every 20 cycles. The process used allows starting from a fully turbulent solution.

A typical convergence curve is presented in Fig. 14. For fully turbulent computations, force coefficients can be considered as converged. When taking into account transition during the computation, the convergence rate was less effective, due to the sub-iterative process considered. However, the convergence in the force coefficients was sufficient for an aerodynamic analysis. For the force coefficients, the contribution of the plate has not been considered, only the wing.

Computations have been carried out in parallel mode using 256 processors. On the ONERA scalar computer (SGI Altix ICE 8200 EX), the overall computing time for the evaluation of the two incidences is about 4 sec/cycle (turbulent or transitional) (1 hour for 900 multigrid cycles).
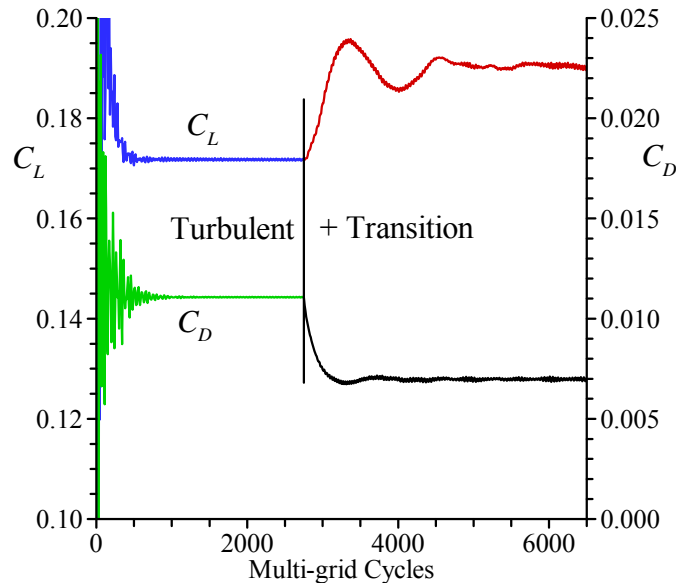


**Figure 14. Typical convergence curves for CFD computations for $\alpha_{geo} = 0$ deg, $Re = 1.6 \times 10^6$ and $M = 0.18$.**

## IV. Results and Discussion

### A. Clean Wing Results
*1. Model Installation Configurations*

As described in Section II.B, the wing model was designed with interchangeable splitter plates and shrouds. The model was also able to mount flush with the floor of the wind-tunnel test section. The splitter plate and shroud geometries and dimensions (cf. Section II.C) were designed based on previous work by Diebold et al.[26] Figure 15 shows a comparison of lift, drag and pitching moment for the four configurations acquired at $Re = 2.4 \times 10^6$ and $M = 0.27$. For angles of attack below stall (less than 13 deg), there was virtually no difference in the coefficients of lift and drag. There were slightly larger differences in pitching moment among the various configurations. In the range

of 4 < α < 13 deg, the configuration with the wing mounted directly at the test-section floor (No Splitter, No Shroud) had a lower $C_M$ than the other three configurations. This was likely the result of the wing root directly interacting with the floor boundary layer. Figure 16 shows a comparison of surface pressure coefficient from the streamwise row of taps closest to the wing root ($y/b = 0.11$) at α = 10.1 deg. There is clearly reduced suction on the wing upper surface on the forward half of this section for the No Splitter, No Shroud configuration. This reduced suction is likely responsible for the slightly lower $C_M$ at this angle of attack.
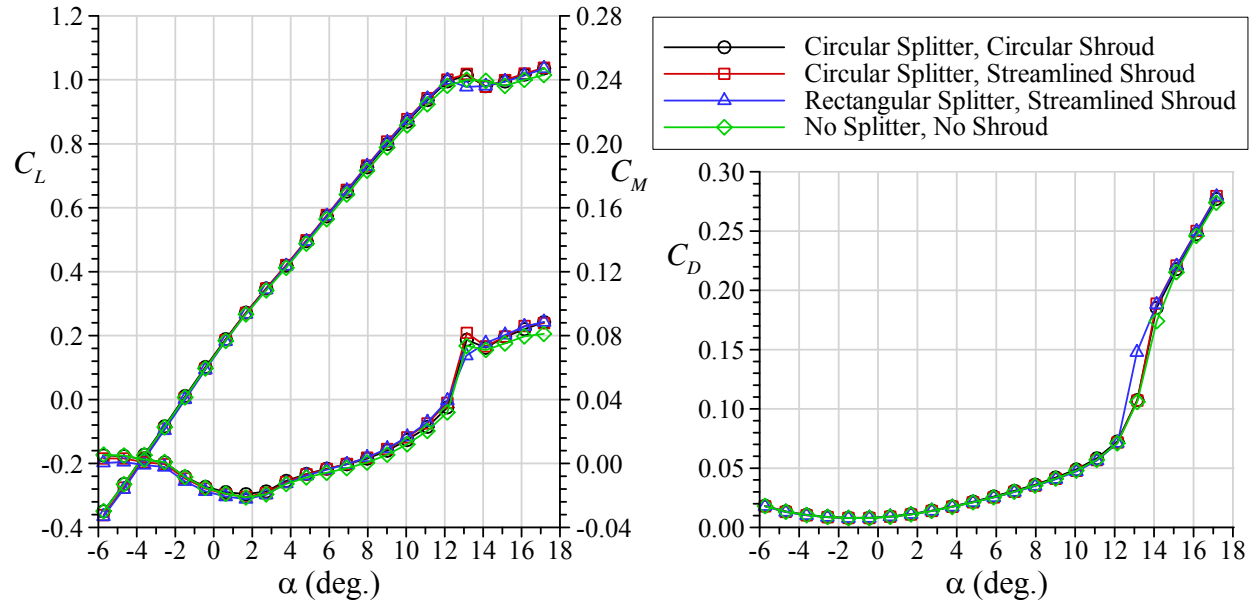


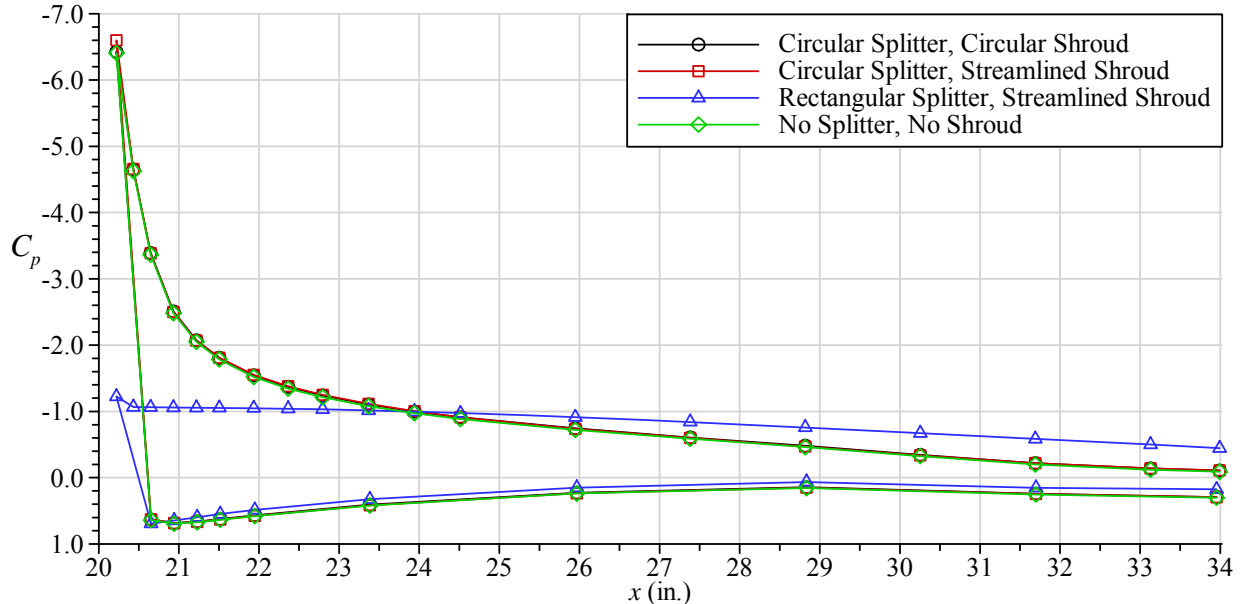**Figure 15. Effect of model installation configuration on clean wing performance at *Re* = 2.4×10⁶ and *M* = 0.27.**
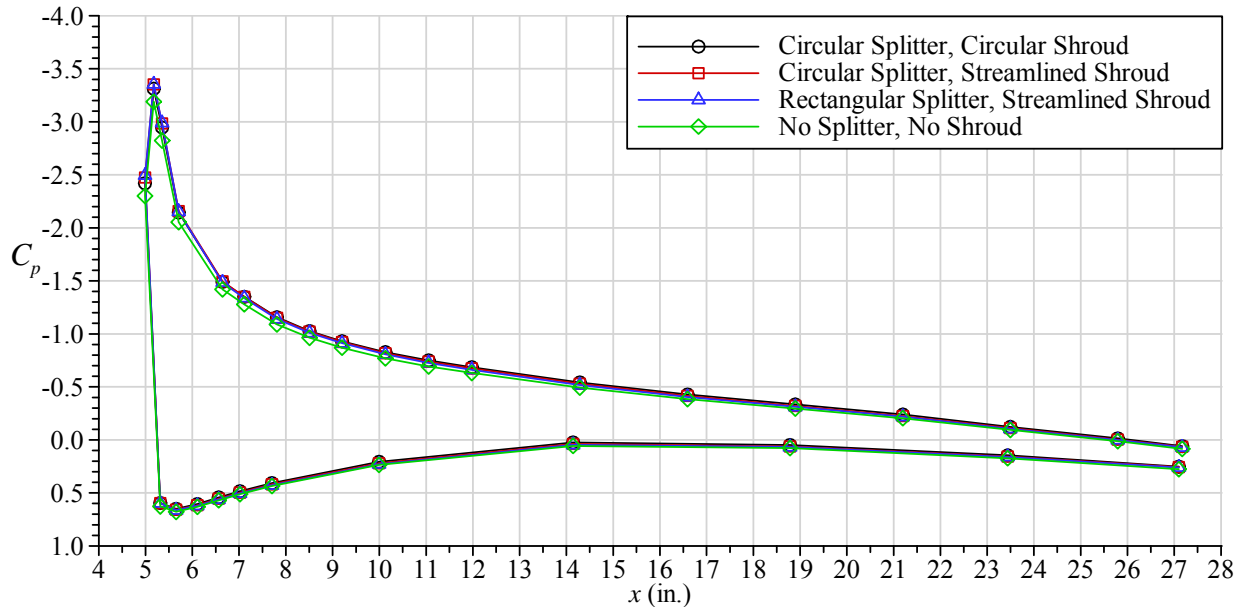


**Figure 16. Effect of model installation configuration on clean wing surface pressure distribution at *Re* = 2.4×10⁶ and *M* = 0.27, *y/b* = 0.11, α = 10.1 deg.**

The performance data in Fig. 15 show more significant differences among the various configurations close to stall at α = 13.2 deg.  At this angle of attack the configuration with the Rectangular Splitter and Streamlined Shroud exhibited the largest difference in performance from the other three.  Surface pressure data on the streamwise tap row near the midspan station (Row 5, *y/b* = 0.44) are plotted for this angle of attack in Fig. 17.  These data clearly show separated flow at this location for the Rectangular Splitter and Streamlined Shroud configuration and attached flow for the other three configurations.  Similar behavior was noted for streamwise pressure rows from Row 3 (*y/b* = 0.28) to Row 7 (*y/b* = 0.60).  These results are consistent with previous work[26] that showed the potential for adverse effects at higher angle of attack for the rectangular splitter plate geometry in smaller scale tests.  Pressure data outboard of Row 7 (*y/b* = 0.60) indicated flow separation for all four configurations.



**Figure 17.  Effect of model installation configuration on clean wing surface pressure distribution at *Re* = 2.4×10⁶ and *M* = 0.27, *y/b* = 0.44, α = 13.2 deg.**

Data like these were generated for the other two Reynolds and Mach number conditions and the comparisons for lift and drag were virtually identical to that shown in Fig. 15.  There was more variation in pitching moment for the various configurations at the other *Re* and *M* conditions.  This variation was not considered significant with respect to the selection of a final model installation configuration for these experiments.

An analysis of these data led to the selection of the installation configuration using the circular splitter plate combined with the streamlined shroud.  As cited in this section, there were some adverse effects associated with rectangular splitter plate at higher angles of attack that led to this being eliminated as a possible configuration.  The mounting of the wing directly at the test section floor (No Splitter, No Shroud) was also eliminated for similar reasons.  In addition, this installation would likely render the data much more unique to this wind-tunnel facility because of the direct influence of the floor boundary layer.  The installation using the circular splitter plate along with the circular shroud yielded aerodynamic performance results that were very similar to the circular splitter plate coupled with the streamlined shroud.  This likely occurred because the overall size of the splitter plate was large compared to the size of either shroud.  There were some minor differences in the aerodynamic data because of the different blockage levels in the flow region between the test-section floor and the splitter plate.  The streamlined shroud was selected because it likely resulted in minimal flow separation in the region between the test-section floor and the splitter plate.  Therefore, the remainder of the data presented in this paper is for the wing installed with the circular splitter plate coupled with the streamlined shroud.

*2. Clean Model Aerodynamics Including Reynolds and Mach Number Effects*

As noted in Section II.A, the WSU wind tunnel operates near atmospheric pressure. Therefore, the Reynolds and Mach numbers cannot be controlled independently. The conditions were selected to yield a two-fold and three-fold increase in both Reynolds number and Mach number from the lowest condition. The aerodynamic performance results for the clean wing at these conditions are plotted in Fig. 18. For these cases, the angle of attack resolution was increased in stall region. For the $Re = 1.6 \times 10^6$ and $M = 0.18$ condition, wing stall was well defined by an abrupt change in all three performance coefficients between α = 13.9 and 14.1 deg, with $C_{L,max} = 1.01$ at $α_{stall} = 13.9$ deg. The same interval of increased angle of attack resolution was also used for the highest Reynolds and Mach number condition. The change in the lift and pitching-moment coefficients was less abrupt at stall, but still well defined with $C_{L,max} = 1.01$ at $α_{stall} = 13.4$ deg. At the lowest Reynolds and Mach number condition, wing stall occurred at a much lower angle of attack based upon the large changes in $C_M$ and $C_D$ between α = 9.0 and 10.0 deg. There was also a distinct change in the lift-curve slope between these angles of attack. For all three conditions, the pitching moment increased significantly approaching stall. This was indicative of flow separation on the outboard portions of the wing. This behavior approaching stall was confirmed in the surface-pressure data and flow visualization presented later in this section.

A stall hysteresis phenomenon was also observed for the clean-model configuration at the two higher Reynolds and Mach number conditions. Performance data were acquired for angle of attack sweeps in which the angle was increased from -5.8 to 17.1 deg, followed by decreasing angles to 0.6 deg. Results are shown in Fig. 19 for the $Re = 1.6 \times 10^6$ and $M = 0.18$ condition. These data exhibit a classic stall hysteresis loop where the flow on the wing was not fully recovered until the angle of attack was decreased to less than 12.1 deg. This behavior has been documented for airfoils and wings operating at Reynolds numbers usually less than $0.3 \times 10^6$ [36-39] although it has also been observed at $Re = 2.2 \times 10^6$.[40] For the case of an airfoil operating at $Re \le 0.3 \times 10^6$, Selig et al.[39] describe the hysteresis as the result of a small laminar separation bubble that remains attached to the airfoil upper surface until stall. This bubble then does not reattach until a lower angle of attack is attained. As described in the following paragraphs, the swept-wing flowfield is characterized by a spanwise-running, leading-edge vortex that is the swept-wing analog of the laminar separation bubble. Stall hysteresis was not observed at the lowest Reynolds and Mach number condition.
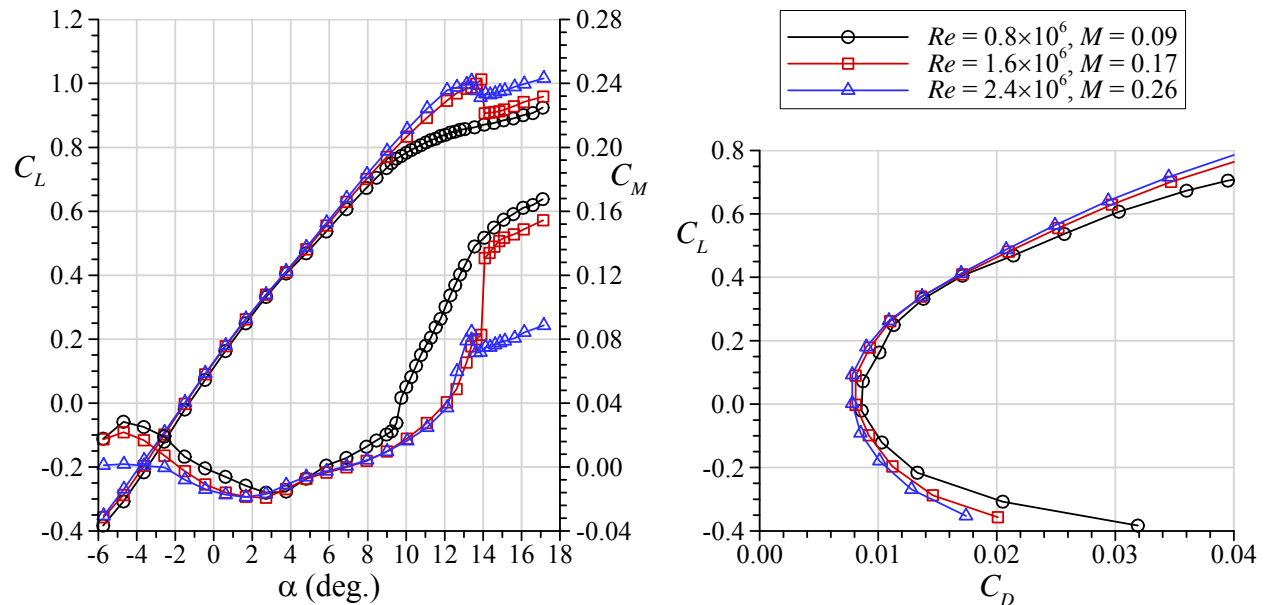


**Figure 18. Effect of Reynolds and Mach number on clean wing performance.**
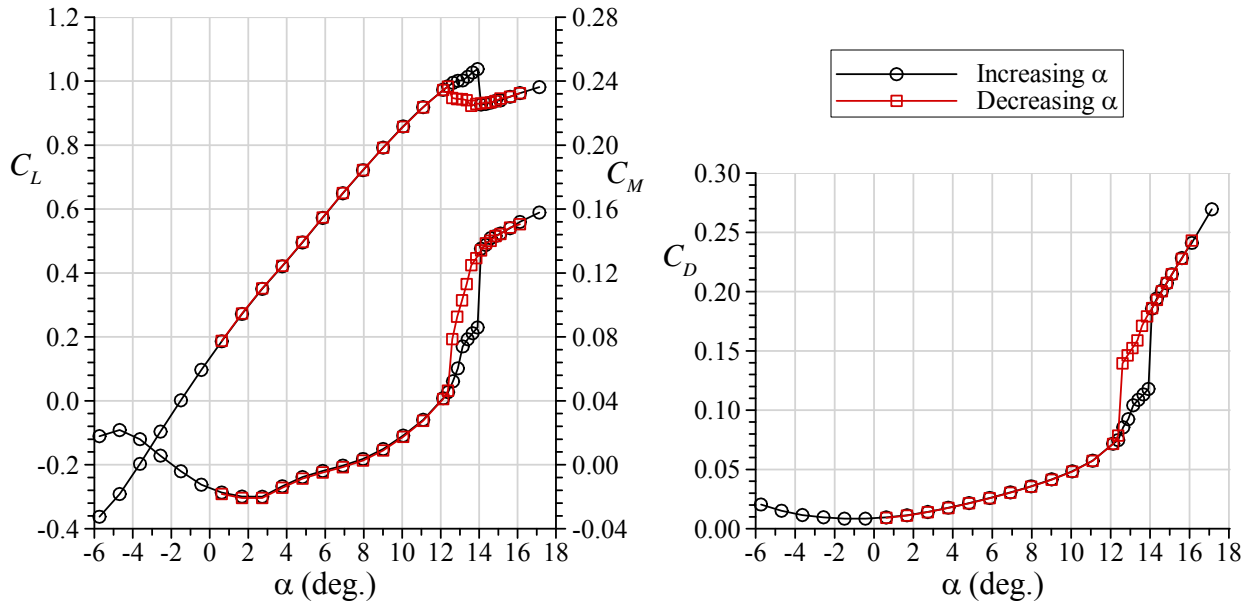
**Figure 19. Effect of increasing and decreasing angle of attack on clean wing performance at $Re = 1.6 \times 10^6$ and $M = 0.18$.**

The performance data for the $Re = 0.8 \times 10^6$ and $M = 0.09$ conditions shown in Fig. 18 exhibited a change in characteristics in the range of $\alpha = 9.0$ to 10.5 deg consistent with wing stall. Figures 20 and 21 show surface-pressure data and flow-visualization images acquired at these conditions. The contours of surface pressure on the wing upper surface were based upon a linear interpolation of the discrete pressure-tap data. The pressure taps used for the interpolation are shown on these plots as small open circles. At $\alpha = 9.0$ deg, the contours of surface pressure exhibited fairly uniform distributions in both streamwise and spanwise directions. The flow visualization image (cf. Fig. 21) shows streamwise flow over most of the model with two exceptions. There appeared to be a small leading-edge vortex near the wing tip that resulted in spanwise flow toward the tip. The vortex was apparently not strong enough to cause an observable change in the local pressure in the contour plot of Fig. 20. There also appeared to be some spanwise flow near the trailing edge on some portions of the wing. Increasing the angle of attack to 10.5 deg, had the effect of stalling the portion of the wing outboard of the Yehudi break ($y = 18.0$ in). There was a distinct change in the upper-surface pressure distribution with decreasing suction toward the wing tip. As mentioned in the previous paragraph, this unloading was consistent with the increase in wing pitching moment shown in Fig. 18. The mini-tuft image in Fig. 21 shows a fairly strong spanwise flow immediately outboard of the Yehudi break with separated flow likely increasing towards the wing tip. This description is consistent with the surface pressure where there was an increase in suction at the leading edge, inboard of the Yehudi break and over the first 30% of the streamwise chord from approximately $y = 18$ to 36 in. Further increases in angle of attack then led to increasing boundary-layer separation on the wing inboard of the Yehudi break. The flowfield for this condition is compared to that of the next highest Reynolds and Mach number in the following paragraph.

The flowfield leading to wing stall for the $Re = 1.6 \times 10^6$ and $M = 0.18$ condition is summarized in the surface-pressure contours and flow-visualization images depicted in Figs. 22 to 25. First in Fig. 22, the surface pressure for $\alpha = 9.0$ and 11.1 deg can be compared and contrasted with the contours shown in Fig. 20 for $Re = 0.8 \times 10^6$ and $M = 0.09$. The pressure coefficients for both conditions at $\alpha = 9.0$ deg look very similar with higher levels of suction being measured for the higher Reynolds and Mach number. As the angle of attack was increased to 11.1 deg for $Re = 1.6 \times 10^6$ and $M = 0.18$, the pressure data in Fig. 22 show that the level of suction continued to increase whereas
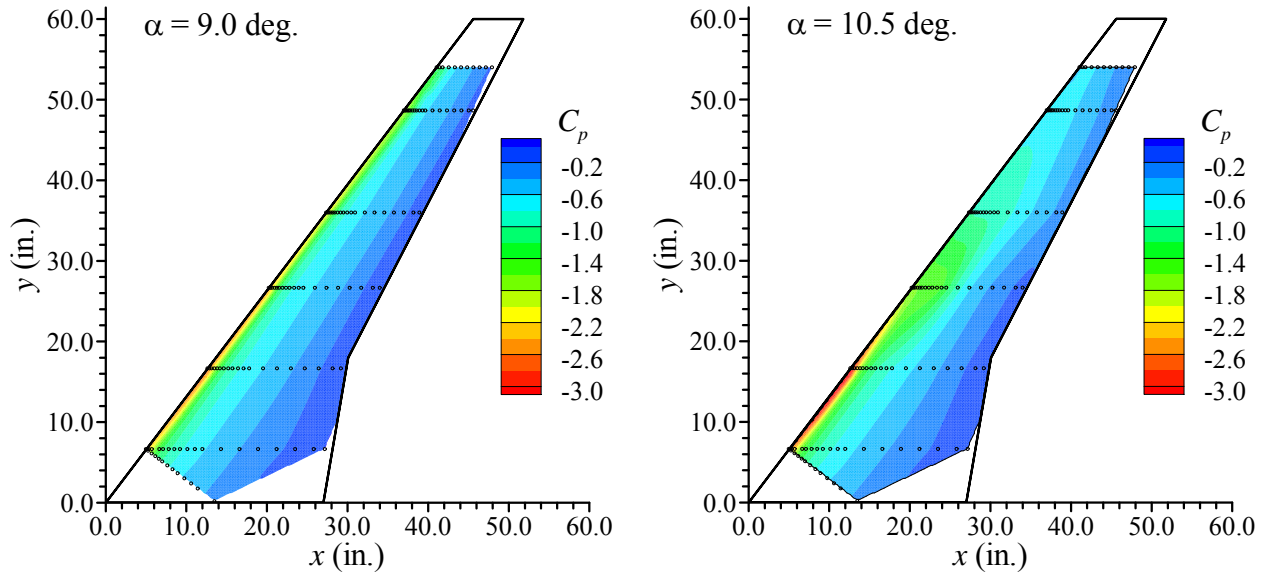
**Figure 20. Contours of upper-surface pressure for α = 9.0 and 10.5 deg at $Re = 0.8 \times 10^6$ and $M = 0.09$.**
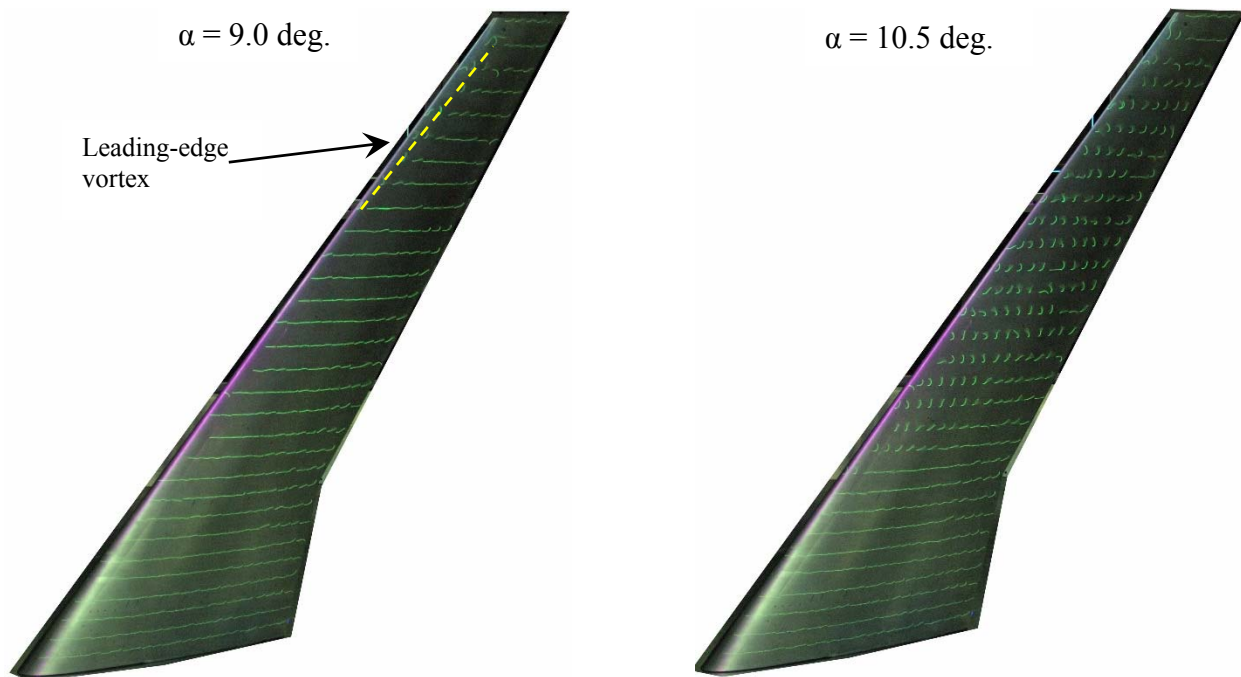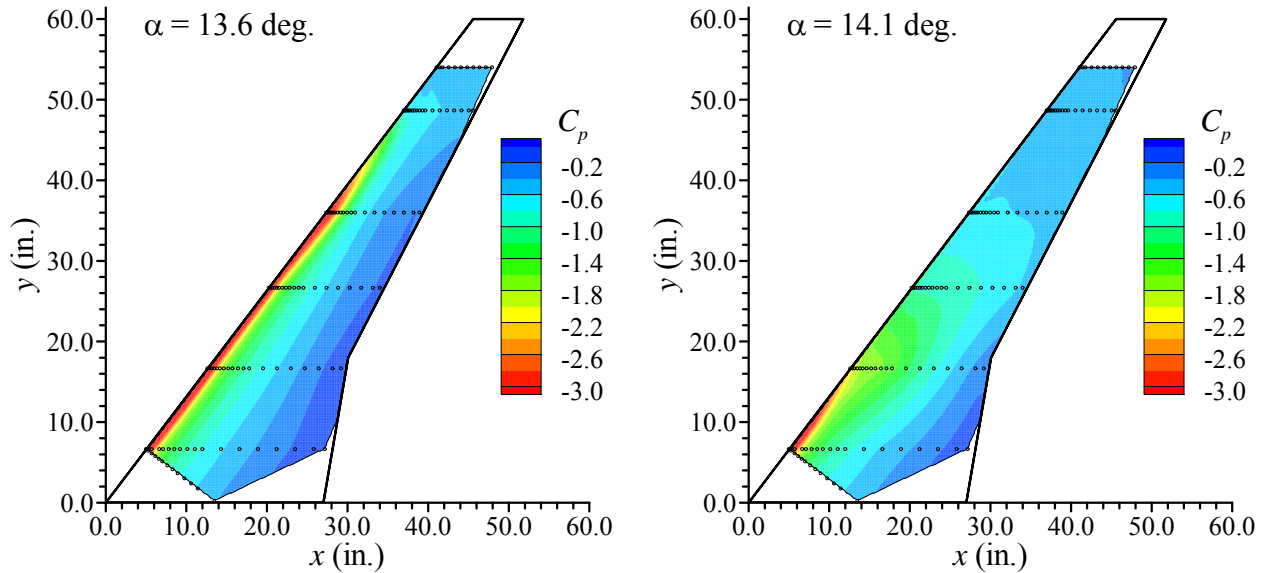


**Figure 21. Mini-tuft flow visualization on upper surface at α = 9.0 and 10.5 deg at $Re = 0.8 \times 10^6$ and $M = 0.09$.**

the wing was already stalled at this angle of attack for the lower Reynolds and Mach number. Figure 23 provides a comparison of the mini-tuft and surface-oil flow visualization methods for α = 11.1 deg. Both images show that a leading-edge vortex separated from the wing surface near the wing tip. The spanwise location where this occurred was slightly more outboard in the mini-tuft image. The separated vortex did not have a measurable effect on the surface pressure shown in Fig. 22. Both images also show the presence of spanwise flow near the wing trailing edge, although difficult to see in the surface-oil flow without zooming into the image. The biggest difference between the images is that the surface-oil flow showed the leading-edge vortex continued inboard along the wing leading edge to the root section. This vortex resulted from laminar separation and the spanwise flow on the wing. The attached vortex ran outboard along the surface resulting in the relatively high levels of suction near the leading edge and significant pressure recovery in the downstream, streamwise direction. In any streamwise, two-

dimensional cut of the upper-surface flowfield, this can be considered analogous to a small, leading-edge laminar separation bubble where the boundary-layer separates, transitions and reattaches to the surface. As the angle of attack was increased to 13.6 deg, the vortex appeared to grow stronger with increased suction near the leading edge, but also separated from the surface at a location farther inboard ($y \approx 45$ inches) as shown in the surface-pressure contour (Fig. 24) and mini-tuft flow visualization (Fig. 25). This high level of suction was not maintained as the angle of attack was increased by 0.5 deg to $\alpha = 14.1$ deg completing the wing stall process. The data in Figs. 24 and 25 for $\alpha = 14.1$ deg show that only a small portion of the wing near the root had attached flow.
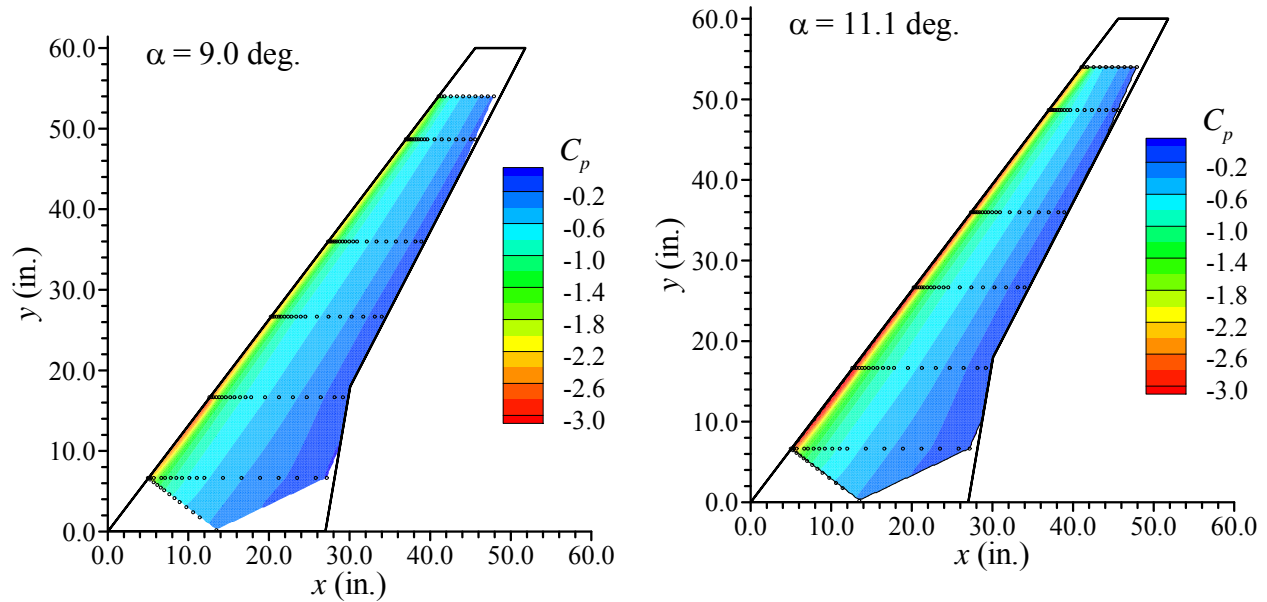


**Figure 22. Contours of upper-surface pressure for $\alpha = 9.0$ and 11.1 deg at $Re = 1.6\times10^6$ and $M = 0.18$.**
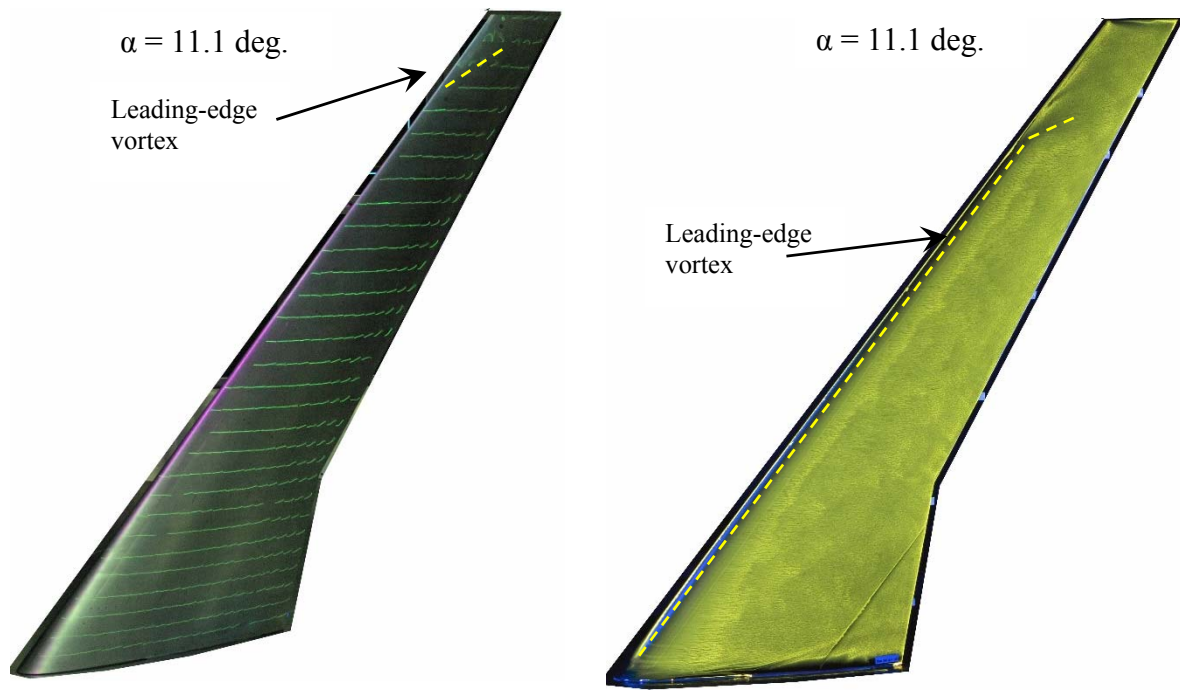


**Figure 23. Comparison of mini-tuft (left) and surface-oil (right) flow visualization on upper surface at $\alpha = 11.1$ deg at $Re = 1.6\times10^6$ and $M = 018$.**

**Figure 24. Contours of upper-surface pressure for α = 13.6 and 14.1 deg at $Re = 1.6 \times 10^6$ and $M = 0.18$.**
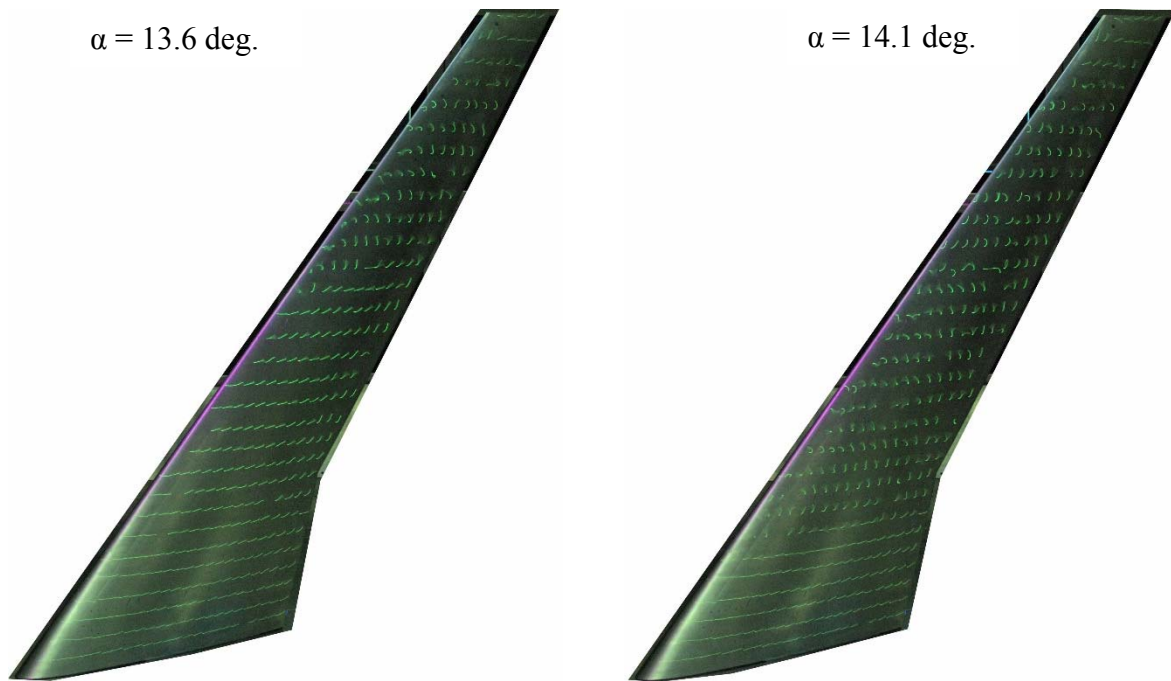


**Figure 25. Mini-tuft flow visualization on upper surface at α = 13.6 and 14.1 deg at $Re = 1.6 \times 10^6$ and $M = 0.18$.**

The flowfield leading to wing stall for the $Re = 2.4 \times 10^6$ and $M = 0.27$ condition was similar to that described in the previous paragraph, with the stalling angle being slightly lower than for $Re = 1.6 \times 10^6$ and $M = 0.18$. The contour of surface pressure for α = 13.1 deg, shown in Fig. 26 for $Re = 2.4 \times 10^6$ and $M = 0.27$ was very similar to that shown previously for $Re = 1.6 \times 10^6$ and $M = 0.18$ at α = 13.6 deg (cf. Fig. 24). This similarity was also observed in the mini-tuft flow visualization images (not shown). Figure 26 also shows the effect of increasing the angle of attack an additional 0.5 deg to α = 13.6 deg where the wing stalls at this Reynolds and Mach number. Here there was a key difference in the stalled flowfield. As shown in Fig. 26 (at α = 13.6 deg), there were higher levels of

suction near $y$ = 50 inches that were not observed for $Re$ = 1.6×10$^6$ and $M$ = 0.18. This increased suction on the outboard section of the wing is consistent with the post-stall decrease in $C_L$ and increase in $C_M$; both of which were not as significant as for $Re$ = 1.6×10$^6$ and $M$ = 0.18 (cf. Fig. 18). While these data provide some interesting insights into the varying combined effects of Reynolds and Mach number on the wing performance, they do not allow for any affirmative conclusion about their independent effects. Data from planned tests in a pressurized wind-tunnel should then allow for these effect to be explored independently, thus providing a further basis to interpret the current results.
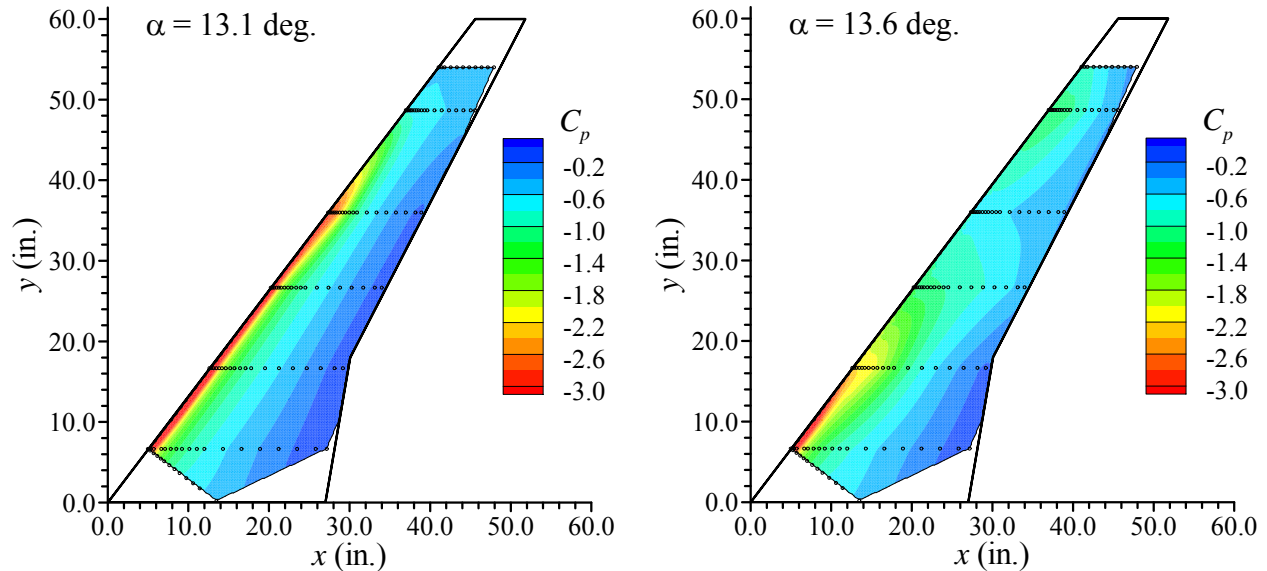


**Figure 26. Contours of upper-surface pressure for $\alpha$ = 13.1 and 13.6 deg at $Re$ = 2.4×10$^6$ and $M$ = 0.27.**

## B. Effect of Boundary-Layer Trips

The geometric details of the boundary-layer trip configurations were described earlier in Section II.D. The effect of these trips on the integrated wing performance data was generally the same for each of the three Reynolds and Mach number conditions. This is illustrated in Fig. 27 for $Re$ = 1.6×10$^6$ and $M$ = 0.18. There was an increase in drag coefficient near zero lift, which is interpreted as a net increase in the wing profile drag due to the trip. At lower and higher values of lift coefficient the induced drag dominated the total drag, thus no further effect of the trip on drag was observed. The pitching moment was also slightly increased in this region of zero to low lift coefficient. More detailed data are required to understand this relatively minor change in the pitching moment in this region. Finally, the data in Fig. 27 show that the trips slightly increased the wing $C_{L,max}$ and stalling angle of attack. There was also a more gradual reduction in lift with some recovery of pitching moment for angles of attack around 14.7 to 16.0 deg. These effects on lift, drag and pitching moment were also observed for the other two Reynolds and Mach number conditions.
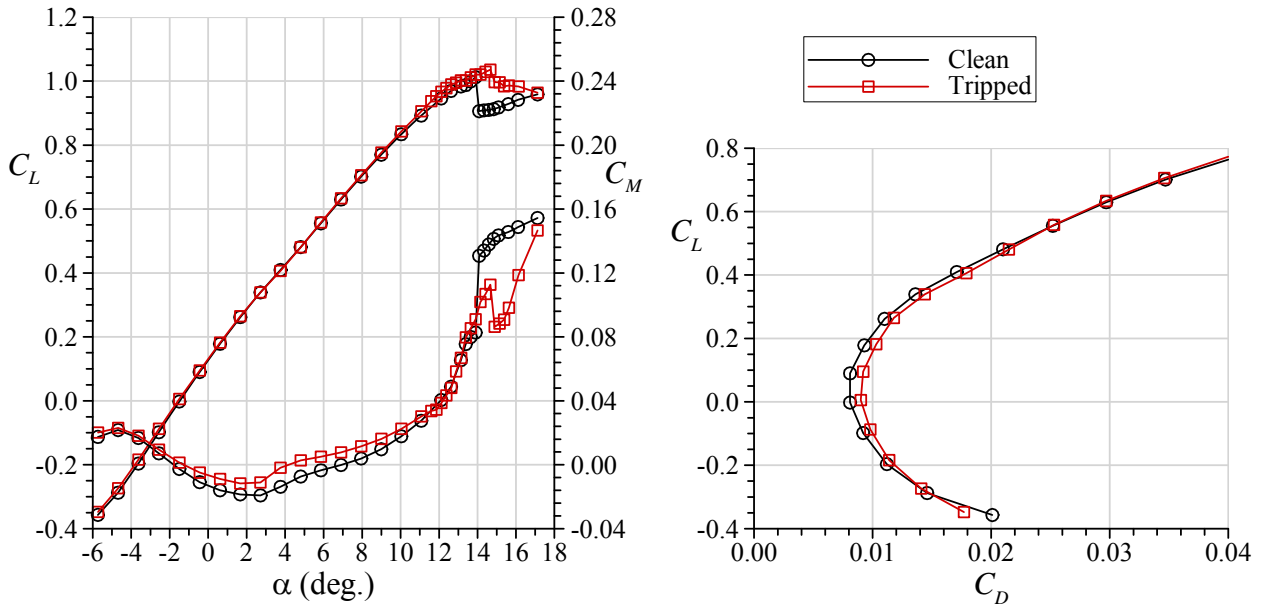
**Figure 27. Effect of upper- and lower-surface boundary-layer trips on wing performance at $Re = 1.6{\times}10^6$ and $M = 0.18$.**

## C. CFD Analysis of Clean Wing Performance

ONERA performed CFD analysis of the clean wing configuration in order to investigate the changes in the wing performance with Reynolds and Mach number described in Section IV.A.2 above. It was noted that for angles of attack greater than about 9 deg, there was a visible change in the wing performance coefficients for the lowest Reynolds and Mach condition in the experimental data (cf. Fig. 18). It is important to know if this behavior is due to pure aerodynamic effects, or if it may be caused by other phenomena. For this range of Reynolds number, the effect of free transition has to be considered. Therefore, both turbulent and transitional computations were carried out with the ONERA elsA software according to the setup described in Section III.

The comparison of computed wing performance coefficients with the experimental data is presented in Figs. 28-30. For these comparisons, the lift coefficient is plotted against the geometric angle of attack, $\alpha_{geo}$, instead of the angle of attack corrected for wind-tunnel wall effects, $\alpha$, used in the previous plots. Even though the CFD setup only included the tunnel floor, much better agreement in the data was obtained for comparisons based upon $\alpha_{geo}$ in place of $\alpha$. This was also confirmed through comparison of surface-pressure profiles between the experimental data and CFD results. The experimental data performance coefficients, $C_L$, $C_D$ and $C_M$, were corrected for wind-tunnel wall effects. For the plots in Figs. 28-30, $C_D$ and $C_M$ are plotted against $C_L$ in order to eliminate the dependence upon angle of attack. The data show that better agreement between the experimental and computational results was obtained when considering computations with free transition compared to turbulent solutions. In particular, the different stall processes for the different flow conditions was captured, even though some improvements are needed for the prediction in absolute value for $Re = 1.6{\times}10^6$; $M = 0.18$ and for $Re = 2.4{\times}10^6$; $M = 0.27$. Note also the good agreement in pitching-moment coefficient between the experimental and CFD results.
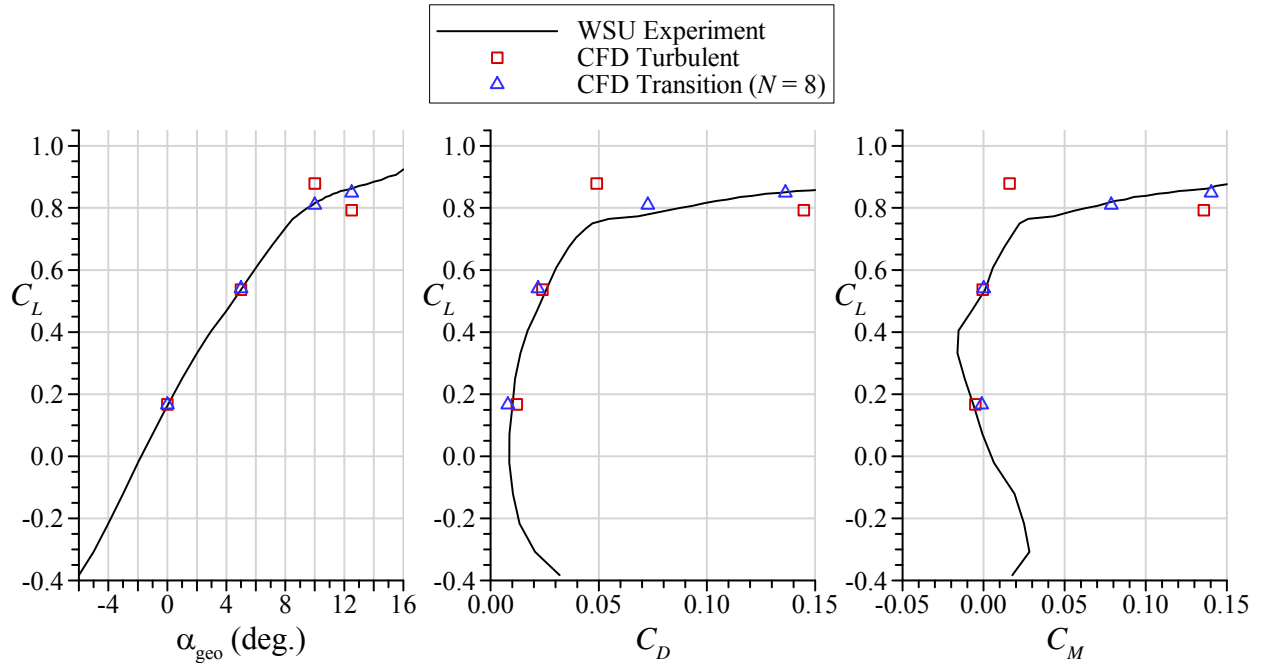
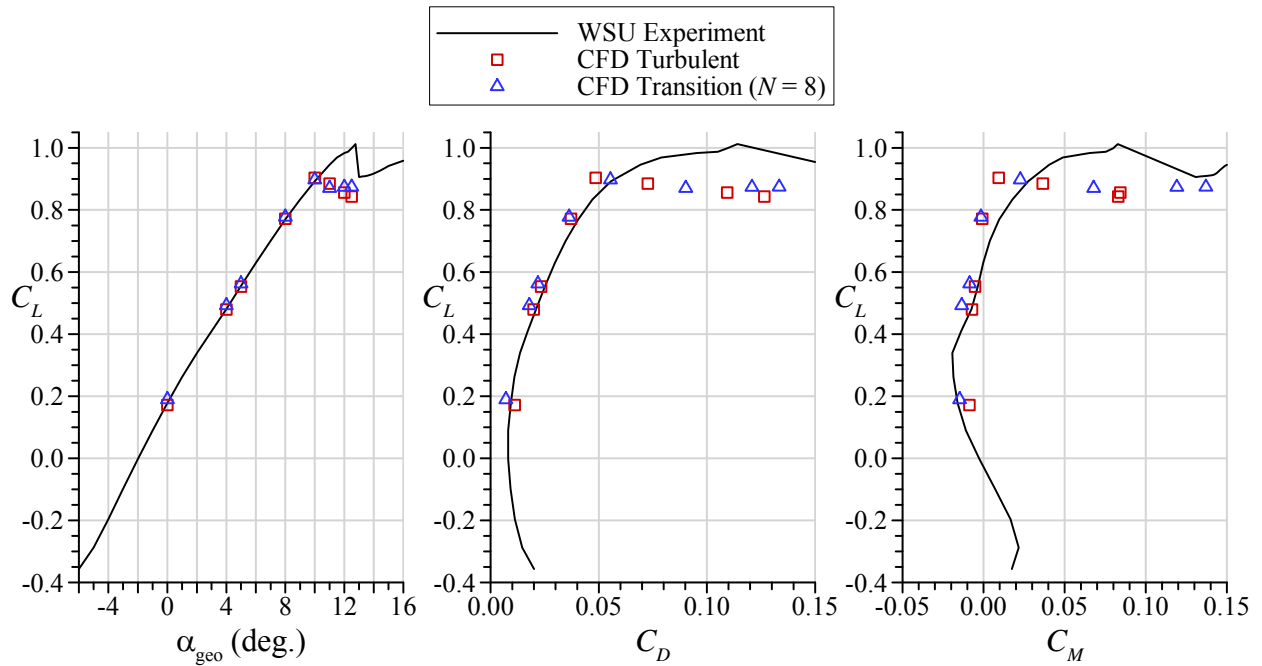**Figure 28.  Comparison of experimental and CFD wing performance results at *Re* = 0.8×10⁶ and *M* = 0.09.**



**Figure 29.  Comparison of experimental and CFD wing performance results at *Re* = 1.6×10⁶ and *M* = 0.18.**
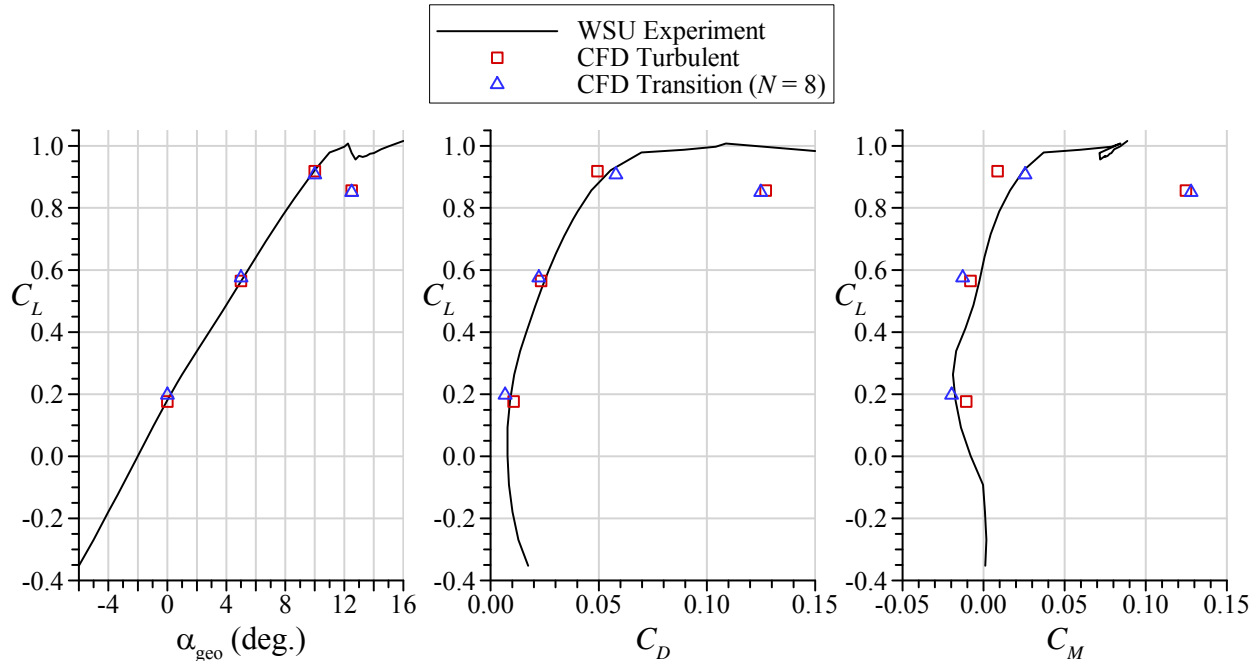
**Figure 30.  Comparison of experimental and CFD wing performance results at $Re = 2.4 \times 10^6$ and $M = 0.27$.**

The effectiveness of the transition model implemented in the CFD analysis was also evaluated by comparison with the surface-oil flow visualization images shown in Fig. 31 for $\alpha_{geo} = 0$ deg and Fig. 32 for $\alpha_{geo} = 4$ deg.  The surface-oil flow image in Fig. 31 was able to capture the approximate transition location variation along the span as indicated in the figure.  There was a distinct change in the amount of oil at the transition location due to the large increase in skin friction that forced more oil downstream on the wing surface.  On the outboard section of the wing, the image was less clear, but seemed to indicate that a laminar-separation bubble with reattachment at the wing trailing edge may have been present.  There was a region of very low shear along the trailing edge, with a line of oil accumulated upstream of this low-shear region and downstream of this low-shear region near the trailing edge.  This
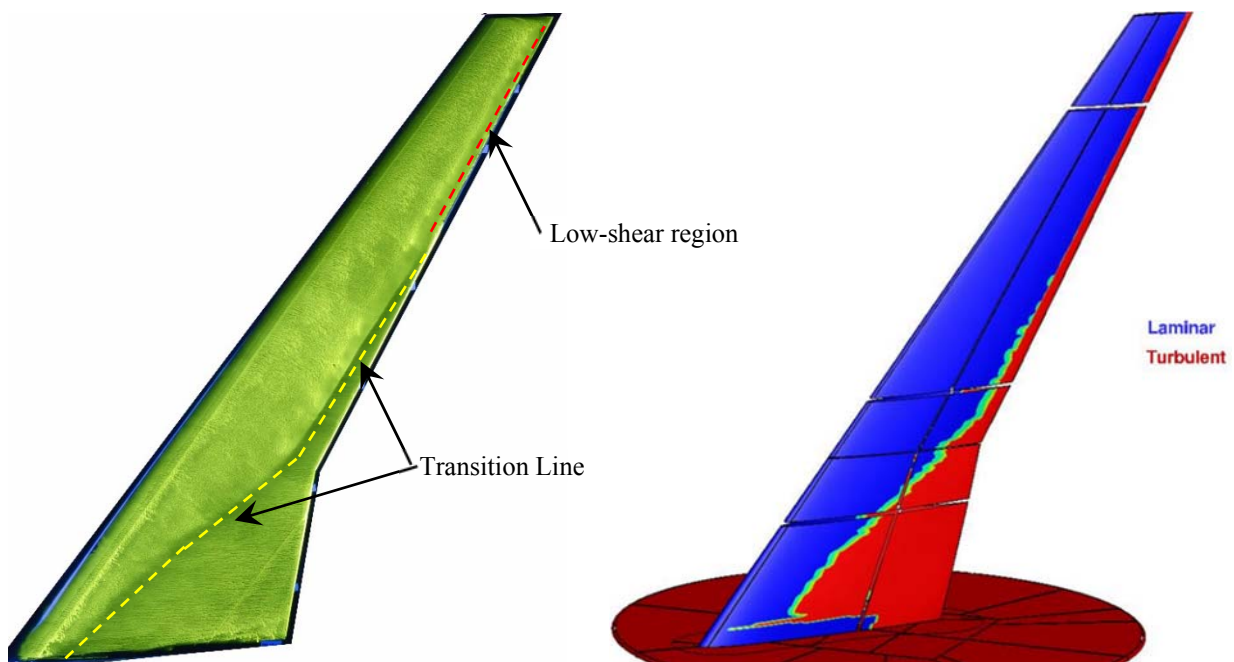


**Figure 31.  Comparison of surface-oil flow visualization (left) with CFD result (free transition) at $\alpha_{geo} = 0$ deg and $Re = 1.6 \times 10^6$ and $M = 0.18$.**
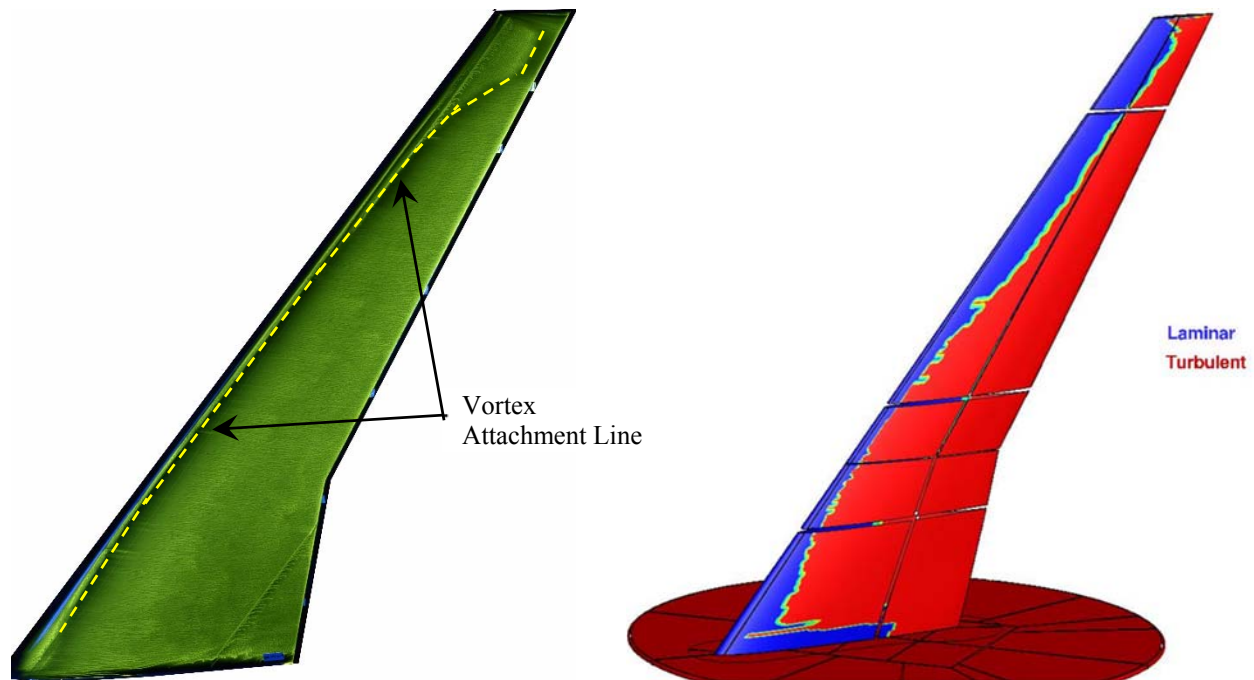
American Institute of Aeronautics and Astronautics

**Figure 32. Comparison of surface-oil flow visualization (left) with CFD result (free transition) at $\alpha_{geo}$ = 4 deg and $Re = 1.6 \times 10^6$ and $M = 0.18$.**

pattern could be indicative of laminar separation, with transition in the separated shear layer followed by reattachment at the trailing edge. Both of these transition features observed in the surface-oil flow compared quite well with the CFD result included alongside for comparison.

Increasing the angle of attack to 4 deg (cf. Fig. 32) had the effect of shifting the transition location much farther upstream on the wing. There was evidence in the surface-oil flow image of laminar separation near the leading edge with subsequent reattachment. As described in Section IV.A.2, above, the reattachment location on a swept-wing is more like a leading-edge vortex because of the influence of the spanwise flow. This vortex laid approximately parallel to the leading edge along most of the span except for the tip region where transition appeared to move farther downstream. This interpretation of the surface-oil flow is qualitatively similar to the CFD result shown in Fig. 32 for comparison. It is also interesting to note that the changes in the flowfield between 0 and 4 deg were consistent with the performance data shown in Fig. 29 where there was a change in the lift-curve slope near $\alpha_{geo} = 2$ deg and a local minimum in the pitching moment. These changes in the integrated performance may reflect the shift in transition location from farther downstream at $\alpha_{geo} = 0$ deg to locations much closer to the leading edge at $\alpha_{geo} = 4$ deg. The data in Fig. 27 show some differences in $C_M$ between the clean and tripped configurations. These small differences in $C_M$ between the clean and tripped wing were comparable to the differences observed between the free transition and turbulent CFD results for $\alpha_{geo} = 0$ and 4 deg.

It was noted earlier in this section that the CFD analysis successfully captured the changes in the onset of wing stall between the $Re = 0.8 \times 10^6$; $M = 0.09$ and the $Re = 1.6 \times 10^6$; $M = 0.18$ conditions. As shown in Fig. 28, the CFD prediction of $C_L$, $C_D$ and $C_M$ for $Re = 0.8 \times 10^6$ and $M = 0.09$ with free transition agrees well with the experimental data. In Fig. 29, the CFD prediction of $C_L$, $C_D$ and $C_M$ for $Re = 1.6 \times 10^6$ and $M = 0.18$ exhibits the proper trend compared to the experimental data, but improvement of the absolute values is needed. As described in Section IV.A.2, the wing demonstrates stall hysteresis at this condition. This presents an additional challenge for CFD simulations where the initial conditions are irrespective of the previous angle of attack.

The computed laminar and turbulent areas of the wing are compared for these two conditions at angles of attack near stall in Fig. 33. Also shown in Figs. 34 and 35 are the computed pressure profiles at different wing sections. For both conditions, the wing upper surface was nearly fully turbulent, except in the acceleration region at the leading edge. However, significant differences in the stall behavior are noticed between turbulent and free transition. For $Re = 0.8 \times 10^6$ and $M = 0.09$, the flow was attached on the wing at every section at $\alpha_{geo} = 10$ deg in turbulent flow, whereas the tip sections were stalled for free transition computations similar to the experimental data. The 10 deg geometric angle of attack corresponds to an experimental corrected value of 11.1 deg. This stall

pattern (attached flow inboard, outboard sections stalled) was shown previously in Figs. 20 and 21 for α = 10.5 deg for the experimental data.

For the case of $\alpha_{geo}$ = 12.5 deg at $Re$ = 1.6×10$^6$ and $M$ = 0.18, there was a completely different process in the CFD simulations when considering the turbulent case where the inboard sections were stalled and the outboard sections were attached. This is contrasted against the free transition case where the inboard sections were attached and the outboard sections were stalled, similar to the experimental data. The 12.5 deg geometric angle of attack corresponds to an experimental corrected value of 13.6 deg. The surface-pressure contour and mini-tuft flow visualization were presented for this case in Figs. 24 and 25. Taken together, these results indicate that the experimental evolution of the wing performance coefficients were due to the effect of three-dimensional transition location evolutions with Reynolds number for the experimental flow conditions. This has to be taken into account for future data analysis when comparing the performance of model with artificial ice shapes (reasonably assumed to be 100% turbulent) with the clean case.
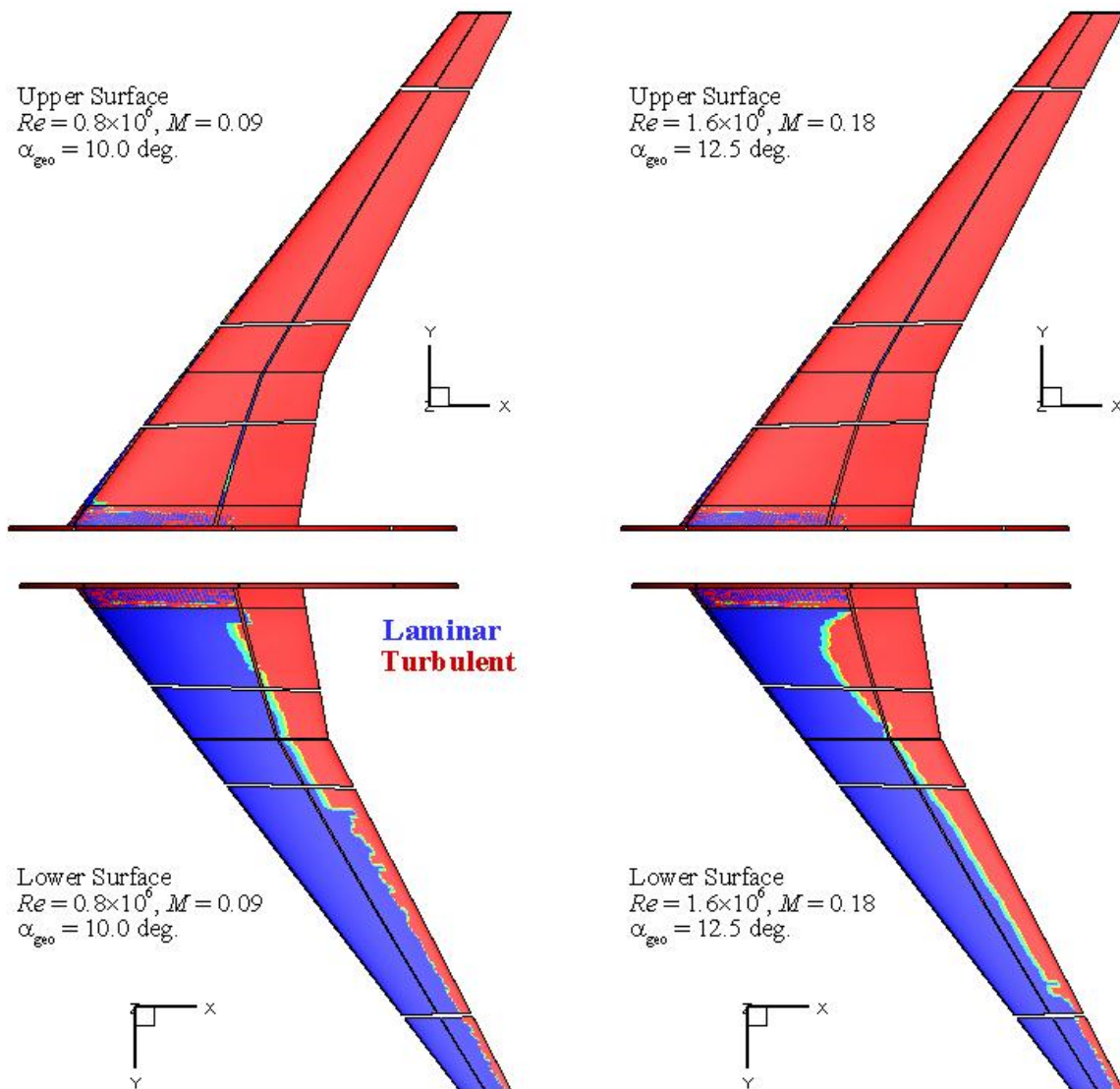


**Figure 33. Comparison of boundary-layer states near stall onset for CFD simulations with free transition.**
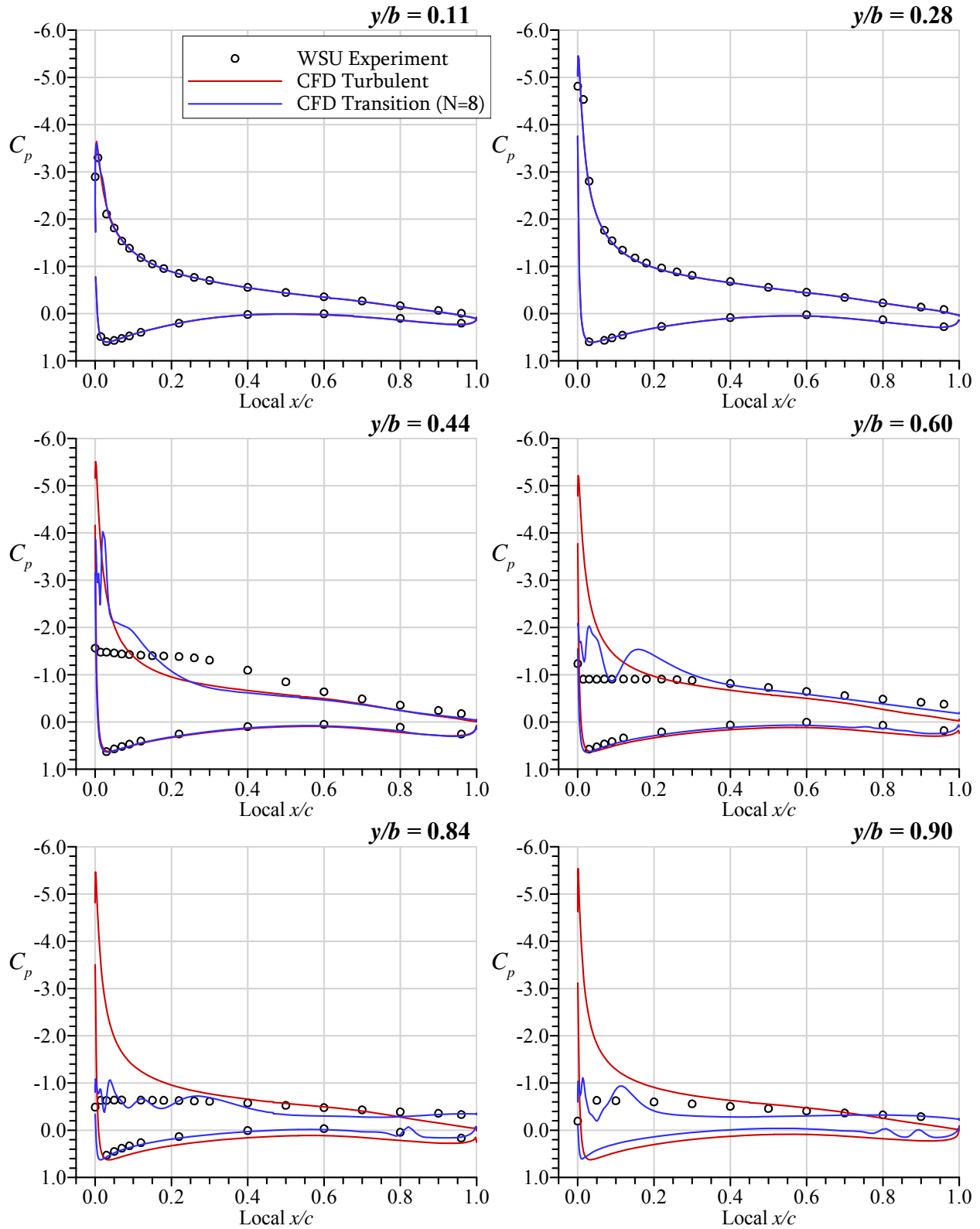
**Figure 34. Comparison of experimental pressure profiles with turbulent and free transition CFD analysis at $\alpha_{geo}$ = 10 deg and $Re$ = 0.8×10⁶ and $M$ = 0.09.**
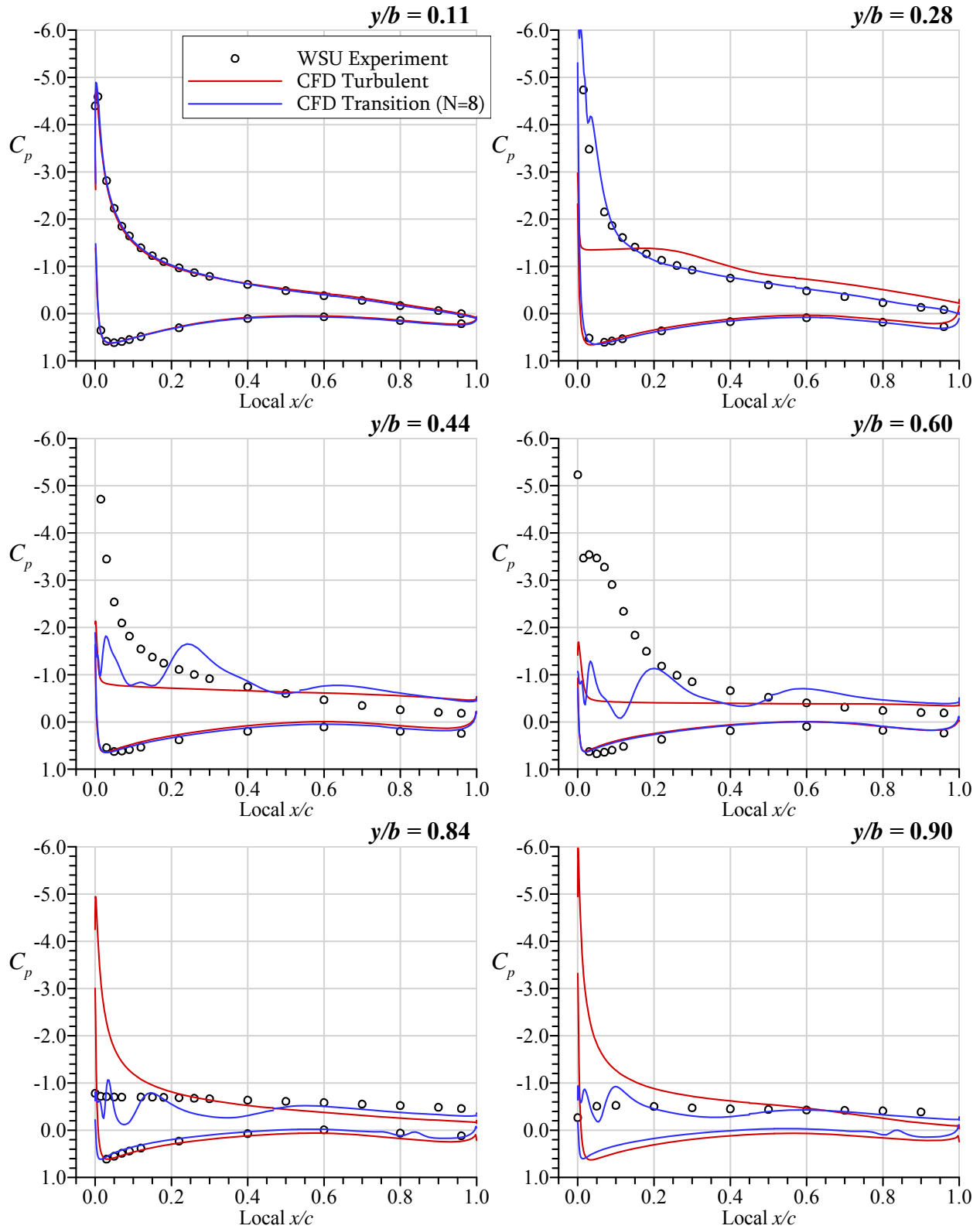
**Figure 35. Comparison of experimental pressure profiles with turbulent and free transition CFD analysis at** $\alpha_{geo} = 12.5$ **deg and** $Re = 1.6 \times 10^6$ **and** $M = 0.18$.

## D. Effect of Artificial Ice Roughness

The artificial ice roughness configurations described in Section II.E. were installed on the wing and subjected to aerodynamic performance testing at the three Reynolds and Mach number conditions used for the clean and tripped wing studies. It was found that Reynolds and Mach number variation had significantly less impact on the performance of the wing with artificial roughness on the leading edge relative to the clean wing. This is illustrated in Fig. 36 for the RPM-based, $k = 0.010$ in hemispherical roughness. The largest difference in the performance coefficients occurred for $C_M$ for angles of attack less than 4 deg. at $Re = 0.8 \times 10^6$ and $M = 0.09$. There was also some variation in $C_D$ near zero lift thus signaling changes in the profile drag due to Reynolds and Mach number. It is interesting to note that for the higher two Reynolds and Mach number conditions, the roughness had the effect of a nearly constant $C_M \approx 0$ from $\alpha$ = -6 to 6 deg. Similar results were obtained for the other artificial ice roughness configurations. The lack of Reynolds and Mach number effect on the wing performance with large, leading-edge roughness is consistent with previous research conducted mostly on straight wings and airfoils (e.g., Ref. 11). Therefore, the aerodynamic data presented in the remainder of this section is for the $Re = 1.6 \times 10^6$ and $M = 0.18$ condition.
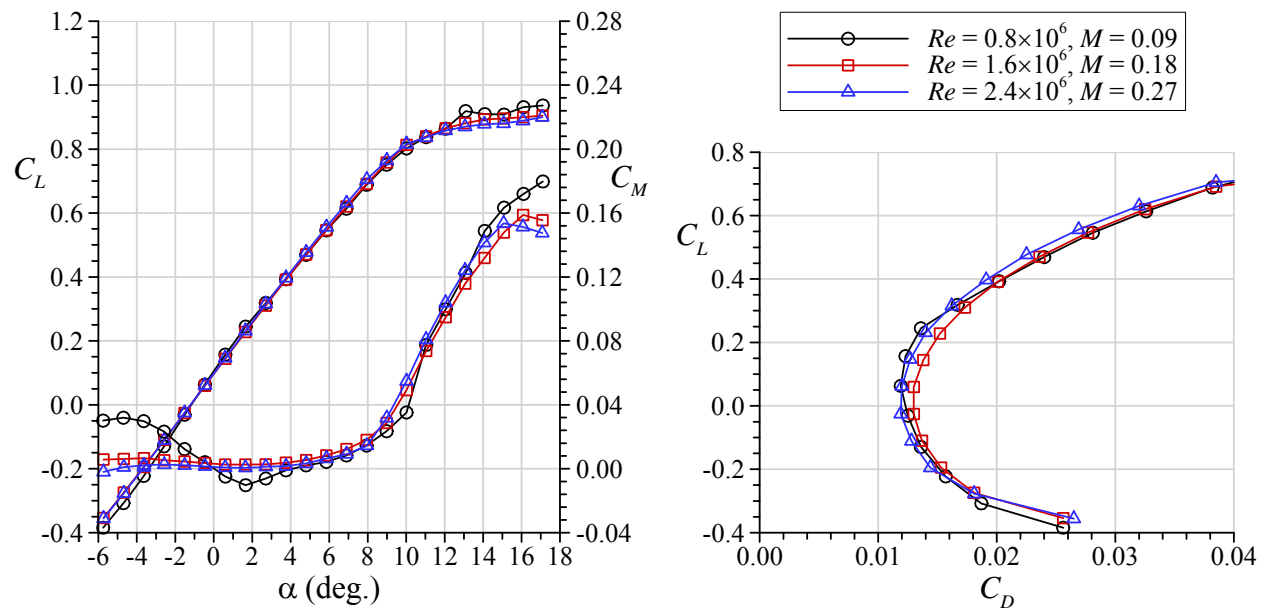


**Figure 36. Effect of Reynolds and Mach number on wing performance with RPM-based, $k = 0.010$ in artificial ice roughness.**

The RPM-based artificial roughness modeled ice roughness as a regular pattern of equally sized and spaced hemispheres. The height, $k = 0.010$ in was determined to be the minimum size that could feasibly be manufactured using standard RPM approaches. An additional larger size of $k = 0.020$ in was also manufactured and tested for comparison. The aerodynamic performance results are summarized in Fig. 37 and compared against the clean wing for the $Re = 1.6 \times 10^6$ and $M = 0.18$ condition. The adverse effect of the roughness is clearly seen and is very distinct from the clean-wing performance. These trends are consistent with typical ice-contaminated wing effects where the larger size resulted in lower $C_L$ (higher angle of attack region) and higher $C_D$. The near-constant $C_M \approx 0$ effect of the roughness is contrasted with the variation in the clean-wing $C_M$ over the range of $\alpha$ = -6 to 6 deg. In the previous section, it was noted that the variation in the clean wing pitching moment over this range was likely caused by the upper-surface, boundary-layer-transition location moving forward to the leading edge from aft sections of the wing. The fact that the leading-edge roughness has eliminated this variation in the pitching moment suggests that the transition location was fixed by the roughness over this angle of attack range. As the angle of attack was increased toward stall, $C_L$ for the wing with roughness gradually decreased relative to the clean wing value beginning around $\alpha$ = 9 deg. The contour plot of surface pressure in Fig. 38 shows a distribution similar to the clean wing in Fig. 22. The main difference appeared to be lower values of the suction peak near the leading edge for the wing with roughness. Surface-oil flow visualization on the wing with roughness shown in Fig. 39 did not reveal any regions of separated flow, although there was evidence of spanwise flow near the wing trailing edge. Other disturbances to the flowfield are evident in Fig. 39 and are labeled. On the outboard half of the wing, the seams between the segments

of the RPM-based roughness affected the flow pattern in the oil. In addition, even the discontinuity in the artificial roughness pattern due to the pressure taps changed the surface flow. Several of the hemispherical roughness elements were removed from the regular pattern around each of the pressure taps (e.g., see Figs. 8 and 9). The interface between the RPM-based roughness segments was a different design for the outboard sections versus the inboard sections, so this may explain why the effect of the seams was only obvious on the outboard portion of the wing. Some of these artifacts persisted as the angle of attack was increased to 11.0 deg. However, the flow over most of the wing outboard of the Yehudi break was separated. There was evidence of three leading-edge vortex formations that propagated some distance downstream before separating from the surface. The vortices did have an effect on the distribution of surface pressure shown in Fig. 38 at $\alpha$ = 11.0 deg where localized increases in the suction peak near the leading edge was observed approximately corresponding to the vortex locations in the surface oil-flow image.
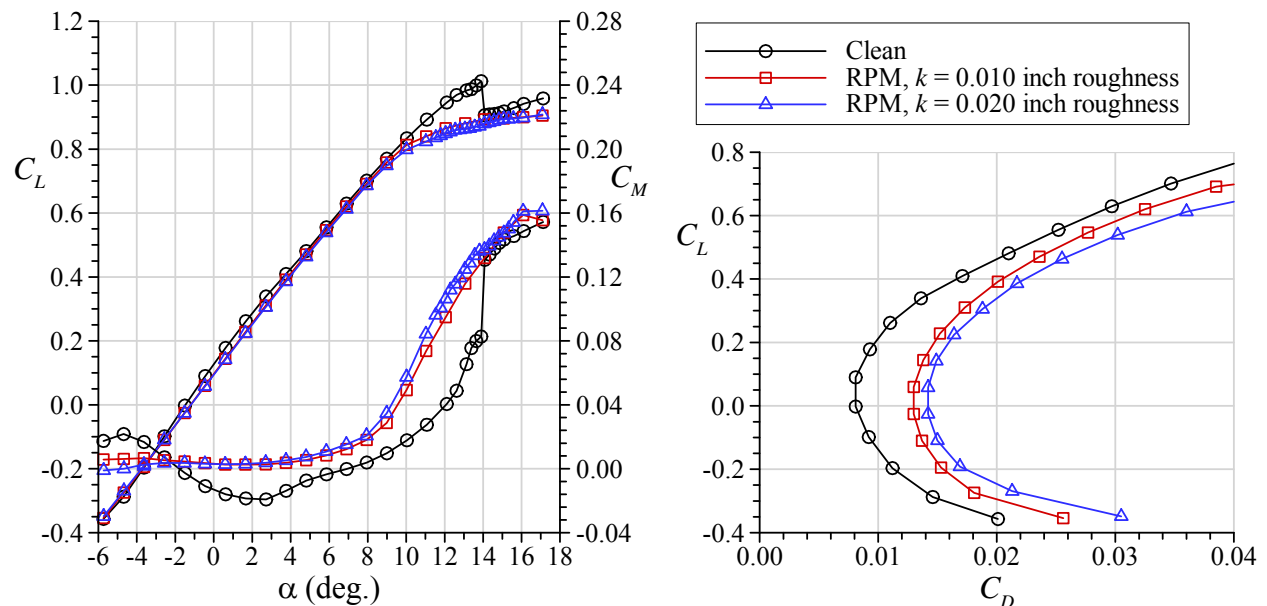


**Figure 37. Effect of RPM-based artificial ice roughness on wing performance at $Re$ = 1.6×10$^6$ and $M$ = 0.18.**
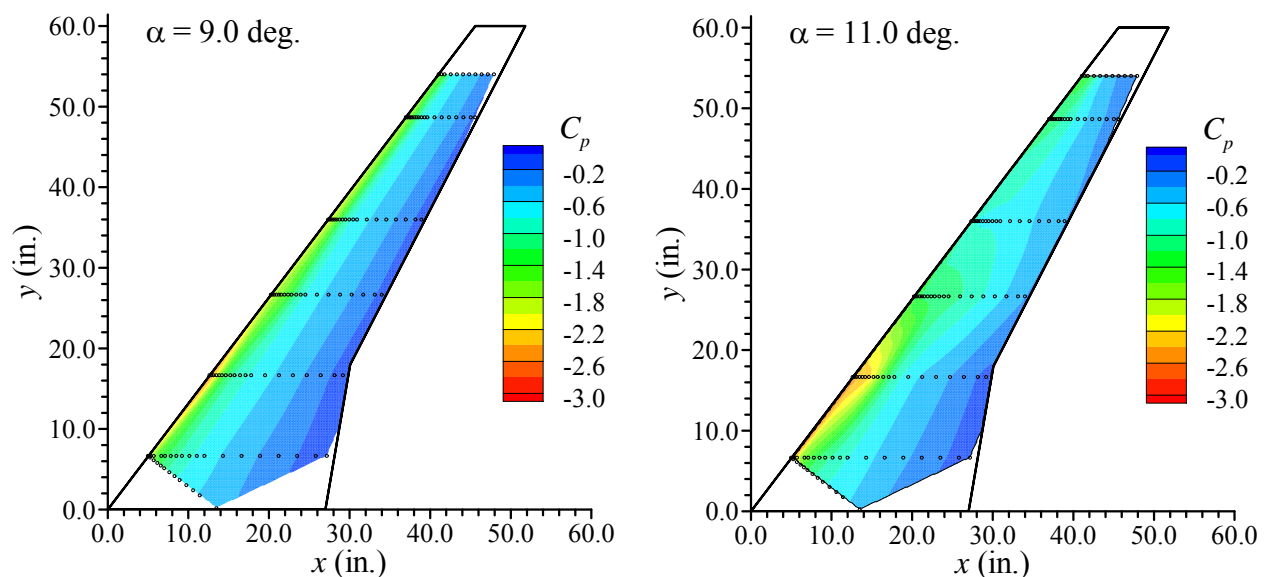


**Figure 38. Contours of upper-surface pressure for the wing with RM-based, $k$ = 0.010 in artificial ice roughness for $\alpha$ = 9.0 and 11.0 deg at $Re$ = 1.6×10$^6$ and $M$ = 0.18.**
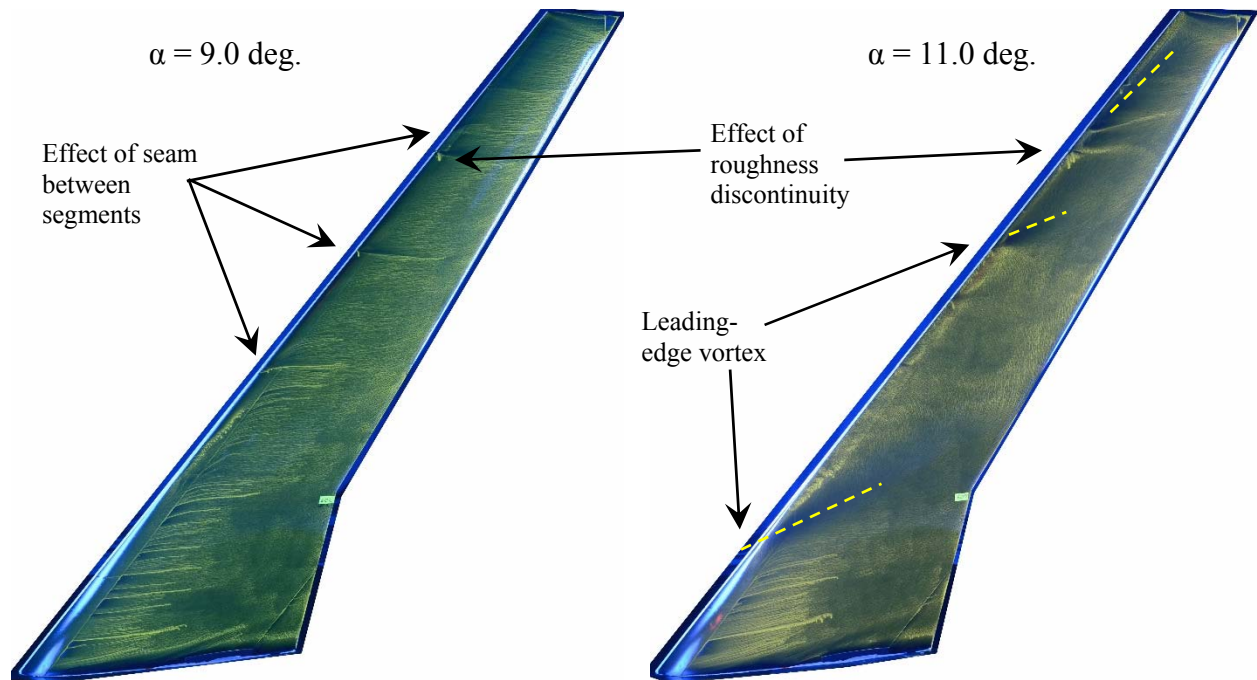
**Figure 39. Surface-oil flow visualization on upper surface for the wing with RPM-based, $k = 0.010$ in artificial ice roughness for $\alpha = 9.0$ and 11.0 deg at $Re = 1.6 \times 10^6$ and $M = 0.18$.**

Aerodynamic tests were also conducted using silicon-carbide grains to represent ice roughness. The grit sizes were selected to approximately match the roughness heights used for the RPM-based configurations. Of course, the geometric morphology of silicon carbide grains tends to be "crystalline" or "faceted" which is significantly different from the hemispherical geometry of the RPM-based roughness. In addition to this difference, the grit size represents some distribution whereas the RPM-based roughness was uniform in size. Because of these differences, it was not expected that the performance of the grit-based roughness would exactly match that of the RPM-based roughness. These methods simply represent two different approaches to simulating real ice roughness which is neither completely hemispherical nor "faceted," but does have some distribution of sizes.

The effect of the three different grit-based roughness sizes on the wing performance is summarized in Fig. 40. For these results it should be noted that there were spanwise gaps or breaks in the roughness near the pressure taps to allow for measurement of surface pressure. An additional, smaller roughness size ($k = 0.005$ in) configuration was also tested. In general, the results were overall consistent with the RPM-based roughness configurations shown in Fig. 37. For example, increasing grit size tended to result in larger aerodynamic penalty. There were some smaller differences. For example, the increases in $C_D$ near zero-lift over the range of grit size was not as large as for the RPM-based equivalent. The most significant difference occurred as the angle of attack was increased into the stall region, $\alpha > 9$ deg. This was readily observed in the $C_M$ data where there was no clear trend in the data.

Further insight was gained by performing a direct comparison of the performance effects of the RPM- and grit-based roughness as shown in Fig. 41 for the $k = 0.010$ in size. An additional configuration plotted in Fig. 41 is the grit-based roughness with no spanwise gaps at the pressure rows. For this configuration, there was a continuous spanwise extent of roughness from root-to-tip which is a better representation of the RPM-based roughness. This had the disadvantage of covering the pressure taps. The aerodynamic data for these configurations exhibited excellent agreement up to about $\alpha = 9$ deg where $C_L$ and $C_M$ data began to diverge. In this region, the data did agree better for the RPM-based roughness and the grit-based roughness with no spanwise gaps. This indicates that the spanwise gaps used for the grit-based roughness in Fig. 40 may have contributed to the anomalous high angle of attack behavior. It was concluded that the wing performance could be very sensitive to spanwise discontinuities in the leading-edge region and this was an important factor in the design of artificial ice shapes for future test campaigns. This result partly led to the improvement implemented in later artificial ice-shape designs where the number of leading-edge segments was reduced from six to two. This is noted in the companion papers by Camello et al.[18] and Lum et al.[19] The data show that RPM-based artificial roughness can generate aerodynamic performance effects comparable to grit roughness of equivalent size when proper care is exercised in design and installation.
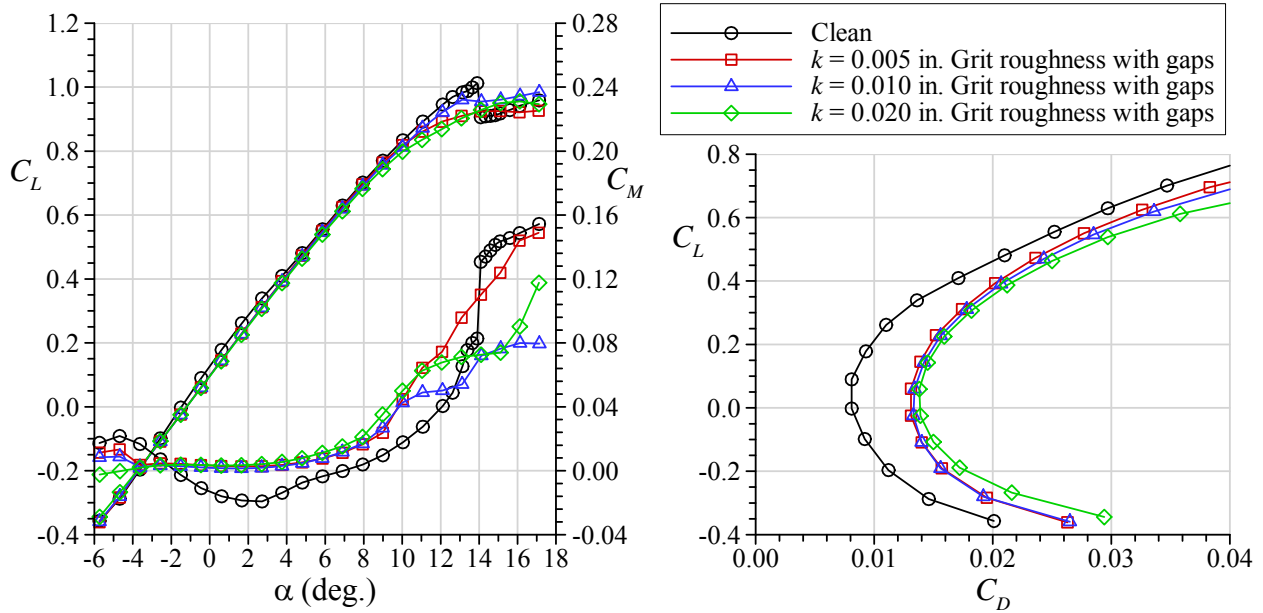
**Figure 40. Effect of silicon-carbide grit artificial ice roughness with gaps cut out around pressure taps on wing performance at $Re = 1.6 \times 10^6$ and $M = 0.18$.**
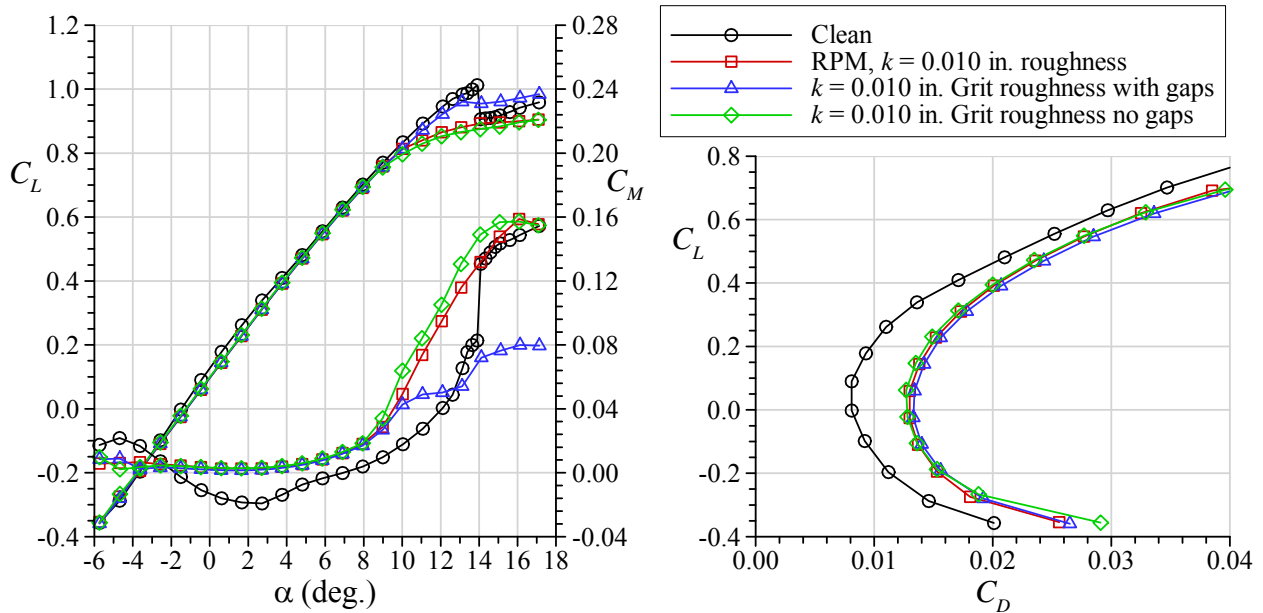


**Figure 41. Comparison of wing performance effects of various artificial ice roughness with $k = 0.010$ in at $Re = 1.6 \times 10^6$ and $M = 0.18$.**

## IV. Summary and Conclusions

Wind-tunnel testing and computational flow simulations were carried out for an 8.9%-scale semispan wing based upon the Common Research Model airplane configuration. The wind-tunnel testing was conducted at the Wichita State University 7 ft x 10 ft wind tunnel from Reynolds numbers of $0.8 \times 10^6$ to $2.4 \times 10^6$ and corresponding Mach numbers of 0.09 to 0.27. Wing force and moment data were acquired along with surface-pressure data. These data were supplemented with mini-tuft and surface-oil flow visualization methods. Model mounting configurations composed of various splitter plate and shroud geometries were investigated along with the effect of boundary-layer trips. The model was designed with an interchangeable removable leading-edge section. This feature allowed for the creation of leading-edge sections with artificial ice roughness using stereolithography. Artificial leading-edge

ice roughness was modeled as hemispherical elements of uniform size and spacing.  The smallest size that could be manufactured had height, $k = 0.010$ inches.  An additional, larger size of $k = 0.020$ inches was also tested.  Silicon-carbide grit of equivalent size was also applied directly to the wing leading edge and the results compared to the RPM-based roughness.

Angle of attack sweeps were performed for four different model mounting configurations using a combination of circular and rectangular splitter plates along with circular and streamlined shrouds.  The model was also mounted with no splitter plate such that the root section was flush with the test-section floor.  The results showed that there were no major differences in the wing aerodynamics for these configurations.  It was concluded that the relatively large size of the splitter plates was successful in decoupling the wing aerodynamics from its mounting in the test section.  However, small differences were observed and the circular splitter plate combined with the streamlined shroud was selected to be the baseline configuration for this and future test campaigns.  The circular splitter plate had the advantage of maintaining the same distance between its leading edge and that of the wing regardless of angle of attack.  The streamline shroud minimized the flow blockage in the gap between the splitter plate and the test-section floor.

A detailed study of the clean-wing aerodynamics and stall characteristics was made for Reynolds numbers of $0.8 \times 10^6$, $1.6 \times 10^6$ and $2.4 \times 10^6$ with corresponding Mach numbers of 0.09, 0.18 and 0.27.  At the lowest Reynolds and Mach number, the wing stalled between $\alpha = 9.0$ and 10.5 deg at a lift coefficient around 0.8.  Increasing the Reynolds and Mach number to $1.6 \times 10^6$ and 0.18 resulted in an increase in the stall angle to 13.9 deg. with $C_{L,max} = 1.01$.  At this condition the stall was characterized by a sharp decrease in lift and increase in pitching moment.  The surface-pressure and flow-visualization data confirmed that the flow over the outboard sections of the wing separated as the wing stalled with the inboard section maintaining attached flow.  Similar behavior was observed at $Re = 2.4 \times 10^6$ and $M = 0.27$, with the stall angle being slightly reduced to 13.6 deg.  It was also noted for the higher two Reynolds and Mach number conditions that a stall hysteresis existed where the flow remained separated until the angle of attack was reduced approximately 2 deg less than the stall angle.  More data from planned tests in a pressurized wind-tunnel are needed to determine the independent effects of Reynolds and Mach number, thus providing a further basis to interpret the current results.

Computational flow simulations were carried out for the baseline clean wing configuration modeling the circular splitter plate and the test-section floor (represented computationally as a symmetry plane), but not including the shroud nor the other tunnel walls.  The flow solver was the ONERA elsA software that solves the compressible, three-dimensional RANS equations.  The one-equation Spalart-Allmaras turbulence model with Quadratic Constitutive Relation correction was used.  The computations were carried out in either fully turbulent mode or with natural transition.  Better agreement between the experimental and computational results was obtained when considering computations with free transition compared to turbulent solutions.  In particular, the different stall processes for the different flow conditions were captured, even though some improvements are needed for the prediction in absolute value for $Re = 1.6 \times 10^6$; $M = 0.18$ and for $Re = 2.4 \times 10^6$; $M = 0.27$.  These results indicate that the experimental evolution of the wing performance coefficients were due to the effect of three-dimensional transition location and that this must be taken into account for future data analysis.  The CFD results also indicated that the magnitude of the wind-tunnel-wall correction on the experimental angle of attack was likely too large as better comparisons were achieved when comparing CFD and experimental data based upon geometric angle of attack.  The magnitude of the wind-tunnel-wall correction on the wing performance coefficients appeared to be much more reasonable.  Additional experimental data from the planned high-Reynolds number tests will provide further basis for comparison.

Aerodynamic performance measurements and flow visualization were conducted with various configurations of artificial ice roughness applied to the wing leading edge.  The adverse effect of the roughness on the wing aerodynamics was consistent with typical ice-contaminated wing effects with lower lift in the stall region and higher profile drag.  Reynolds and Mach number variation had significantly less impact on the performance of the wing with artificial roughness on the leading edge relative to the clean wing.  Leading-edge roughness did not alter the general clean-wing stall pattern where there outboard sections of the wing stalled first while flow on inboard sections near the root remained attached.  This research confirmed that small-scale ice roughness with height $k = 0.010$ in could be designed and built using rapid-prototype manufacturing methods.  This conclusion was verified through comparison with traditional grit roughness that is often used to simulate ice roughness.  Additionally, it was found that the method of applying grit to the wing surface had a relatively large impact on the aerodynamics.  It was concluded that the wing performance could be very sensitive to spanwise discontinuities in the leading-edge region and this should be an important factor in the design of artificial ice shapes for future test campaigns.  This result partly led to the improvement implemented in later artificial ice-shape designs where the number of leading-edge segments was reduced from six to two.  The data show that RPM-based artificial roughness can generate

aerodynamic performance effects comparable to grit roughness of equivalent size when proper care is exercised in design and installation. The conclusions of this combined experimental and computational study contributed directly to the successful implementation of follow-on test campaigns with numerous artificial ice-shape configurations for this 8.9% scale model. In addition, these conclusions also greatly facilitated the design and preparations for the planned high-Reynolds number test campaigns using a larger, 13.3% scale model of the same wing. Therefore, this work has contributed to the overall research objectives for improving aerodynamic icing simulation of swept-wing icing effects for current and future aircraft design, certification and safe operation.

## Acknowledgements

## References

[1] Broeren, A.P., Potapczuk, M.G., Riley, J.T., Villiedieu, P., Moens, F., and Bragg, M.B., "Swept-Wing Ice Accretion Characterization and Aerodynamics," AIAA Paper 2013-2824, June 2013, also NASA/TM—2013-216555, Sept. 2013.

[2] Broeren, A.P., Potapczuk, M.G., Lee, S., Malone, A.M., Paul, B.P., Jr., and Woodard, B.S., "Ice-Accretion Test Results for Three Large-Scale Swept-Wing Models in the NASA Icing Research Tunnel," AIAA Paper 2016-3733, June 2016; also NASA/TM—2016-219137, Sept. 2016.

[3] Fujiwara, G.E.C., Bragg, M.B., Camello, S.C., and Lum, C., "Computational and Experimental Ice Accretions of Large Swept Wings in the Icing Research Tunnel," AIAA Paper 2016-3734, June 2016.

[4] Radenac, E., "Validation of a 3D Ice Accretion Tool on Swept Wing of the SUNSET2 Program," AIAA Paper 2016-3735.

[5] Broeren, A.P., Addy, H.E., Jr., Bragg, M.B., Busch, G.T., Guffond, D., and Montreuil, E., "Aerodynamic Simulation of Ice Accretion on Airfoils," NASA/TP—2011-216929, June 2011.

[6] Broeren, A.P, Addy, H.E., Jr., Lee, S., Monastero, M.C., "Validation of 3-D Ice Accretion Measurement Methodology for Experimental Aerodynamic Simulation," NASA/TM—2015-218724, July 2015.

[7] Morgan, H.L., Ferris, J.C., McGhee, R.J., "A Study of High-Lift Airfoils at High Reynolds Numbers in the Langley Low-Turbulence Pressure Tunnel," NASA TM-89125, 1987.

[8] Addy, H.E., Jr., and Chung, J.J., "A Wind Tunnel Study of Icing Effects on a Natural Laminar Flow Airfoil," AIAA Paper 2000-0095, Jan. 2000; also NASA/TM—2000-209775, Jan. 2000.

[9] Addy, H.E., Jr., "Ice Accretions and Icing Effects for Modern Airfoils," NASA/TP-2000-210031, April 2000; also U.S. Dept. of Transportation/Federal Aviation Administration Rept. DOT/FAA AR-99/89, April 2000.

[10] Addy, H.E., Jr., Broeren, A.P., Zoeckler, J.G., and Lee, S., "A Wind Tunnel Study of Icing Effects on a Business Jet Airfoil," AIAA Paper 2003-0727, Jan. 2003; also NASA/TM—2003-212124, Feb. 2003.

[11] Bragg, M.B., Broeren, A.P., and Blumenthal, L.A., "Iced-Airfoil Aerodynamics," *Progress in Aerospace Sciences*, Vol. 41, No. 5, July 2005, pp. 323-418.

[12] Broeren, A.P., Bragg, M.B., and Addy, H.E., Jr., "Effect of Intercycle Ice Accretions on Aerodynamic Performance," *Journal of Aircraft*, Vol. 41, No. 1, Jan.-Feb. 2004, pp 165-174.

[13] Broeren, A.P., Bragg, M.B., Addy, H.E., Jr., Lee, S., Moens, F., and Guffond, D., "Effect of High-Fidelity Ice Accretion Simulations on the Performance of a Full-Scale Airfoil Model," *Journal of Aircraft*, Vol. 47, No. 1, Jan.-Feb. 2010, pp. 240-254; also NASA/TM-2010-216344, Jun. 2010.

[14] Vassberg, J.C., DeHann, M.A., Rivers, S.M., and Wahls, R.A., "Development of a Common Research Model for Applied CFD Validation Studies," AIAA Paper 2008-6919, Aug. 2008.

[15] Rivers, M.B., and Dittberner, A., "Experimental Investigation of the NASA Common Research Model," AIAA Paper 2010-4218, June 2010.

[16] Rivers, M.B., and Dittberner, A., "Experimental Investigations of the NASA Common Research Model in the NASA Langley National Transonic Facility and the NASA Ames 11-Ft Transonic Wind Tunnel," AIAA Paper 2011-1126, Jan. 2011.

[17] Vassberg, J. C., Tinoco, E. N., Mani, M., Rider, B., Zickuhr, T., Levy, D.W., Brodersen, O., Eisfeld, B., Crippa, S., Wahls, R.A., Morrison, J. H., Mavriplis, D.J., and Murayama, M., "Summary of the Fourth AIAA CFD Drag Prediction Workshop," AIAA Paper 2010-4547, June 2010.

[18] Camello, S.C., Bragg, M.B., Broeren, A.P., Lum, C.W., Woodard, B.S., and Lee, S., "Effect of Full-Span, Artificial Ice Shapes on the Performance of an 8.9% Scale Semispan Swept Wing.," AIAA 9th Atmospheric and Space Environments Conference, Denver, CO, June 5-9, 2017 (submitted for publication), 2017.

[19] Lum, C.W., Sandhu, N., Diebold, J.M., Woodard, B.S., and Bragg, M.B., "The Application of a Five-Hole Probe Wake-Survey Technique to the Study of Swept Wing Icing Aerodynamics," AIAA 9th Atmospheric and Space Environments Conference, Denver, CO, June 5-9, 2017 (submitted for publication), 2017.

[20] "Data Reduction System: 3D Reflection Plane Coordinate System Definition, Moment Transfers, Coordinate Rotations," Walter H. Beech Wind Tunnel Engineering Process Description, Rev. A., Apr. 2012.

[21] Coleman, H.W., and Steele, W.G., *Experimentation and Uncertainty Analysis for Engineers*, Wiley-Interscience, New York, 1989, pp.40-118.

[22] Kline, S., and McClintock, F.A, "Describing Uncertainties in Single Sample Experiments," Mechanical Engineering, Vol. 75, No. 1, 1953, pp. 3-8.

[23] Woodard, B.S., Broeren, A.P., Diebold, J.M., and Bragg, M.B., "Preliminary Assessment of Low-Reynolds Number Aerodynamics for a Swept Wing with Artificial Ice Roughness," FAA Technical Report, submitted for publication, Sept. 2015.

[24] Barlow, J.B., Rae, W.H., Jr., Pope, A., *Low-Speed Wind Tunnel Testing*, John Wiley & Sons, Inc., 3rd Ed., 1999, pp. 367-425.

[25] "Data Reduction System: Boundary Corrections Three Dimensional Aircraft," Walter H. Beech Wind Tunnel Engineering Process Description, Apr. 2014.

[26] Diebold, J.M., Woodard, B.S., Monastero, M.C., and Bragg, M.B., "Experimental Study of Splitter Plates for Use with Semispan Wing Models," AIAA Paper 2015-1227, Jan. 2015.

[27] Hue, D., Peron, S., Wiart L., Atinault, O., Gournay, E., Raud, P., Benoit, C., Mayeur, J., "Validation of a near-body and off-body grid partitioning methodology for aircraft aerodynamic performance prediction*," Computer and Fluids*, Vol. 117, 2015.

[28] Benoit, C., Peron, S., Landier, S., "Cassiopee: a CFD pre- and post-processing tool," *Aerospace Science and Technology*, Vol. 45, pp. 272-243, 2015.

[29] Cambier, L., Heib, S., and Plot, S., "The Onera elsA CFD Software: Input from Research and Feedback from Industry," *Mechanics and Industry*, 14(3):159-174, 2013.

[30] Jameson, A., Schmidt, W., and Turkel, E., "Numerical Solutions of the Euler Equations by Finite Volume Methods Using Runge-Kutta Time Stepping," AIAA Paper 81-1259, 1981.

[31] Spalart, P.R., and Allmaras, S.R., "A One-Equation Turbulence Model for Aerodynamic Flows," AIAA Paper 92-0439, 1992.

[32] Moens, F., Perraud, J., Krumbein, A., Toulorge, T., Iannelli, P., and Hanifi, A., "Transition prediction and impact on 3D high-lift wing configuration," *Journal of Aircraft,* Vol. 45 No. 5, Sept.-Oct. 2008, pp. 1751-1766.

[33] Arnal, D., "Transition Prediction in Transonic Flow", IUTAM Symposium "Transsonicum III", Göttingen, Eds. Zierep and Oertel, Springer Verlag (1988), pp 253-262.

[34] Gleyzes, C., Cousteix, J., and Bonnet, J.L., "Theoretical and experimental study of low Reynolds number transitional separation bubbles," Conference on Low Reynolds Number Airfoil Aerodynamics, T.J. Mueller, Editor, UNDAS-CP-77B123, June 1985.

[35] Arnal D., "Three-Dimensional Boundary Layers: Laminar-Turbulent Transition,*" AGARD Report 741 (Computations of three-dimensional Boundary Layers including Separation),* Rhode Saint Genèse (Belgium), 1986.

[36] Mueller, T.J., "The Influence of Laminar Separation and Transition on Low Reynolds Number Airfoil Hysteresis," Journal of Aircraft, Vol. 22, No. 9, Sept. 1985, pp. 763-770.

[37] Marchmann, J.F., III, Chang, Y.K., and Robinson, R.D., "Sweep Effects on Low Reynolds Number Stall Hysteresis," AIAA Paper 88-4419, Sept. 1988.

[38] Marchmann, J.F., III, Sumantran, V., and Schaefer, C.G., "Acoustic and Turbulence Influences on Stall Hysteresis," AIAA Paper 86-0170, Jan. 1986.

[39] Selig, M.S., Guglielmo, J.J., Broeren, A.P., and Giguere, P., "Experiments on Airfoils at Low Reynolds Numbers," AIAA Paper 96-0062, Jan. 1996.

[40] Biber, K., "Stall Hysteresis of an Airfoil with Slotted Flap," AIAA Paper 2005-1230, Jan. 2005.